

The Vertical City Weather Generator (VCWG v1.2.0)

Mohsen Moradi¹, Benjamin Dyer¹, Amir Nazem¹, Manoj K. Nambiar¹, M. Rafsan Nahian¹, Bruno Bueno⁴, Chris Mackey⁶, Saeran Vasanthakumar⁷, Negin Nazarian², E. Scott Krayenhoff³, Leslie K. Norford⁵, and Amir A. Aliabadi¹

¹School of Engineering, University of Guelph, Guelph, Canada

²Built Environment, University of New South Wales, Sydney, Australia

³School of Environmental Sciences, University of Guelph, Guelph, Canada

⁴Fraunhofer Institute for Solar Energy Systems ISE, Freiburg, Germany

⁵Department of Architecture, Massachusetts Institute of Technology, Cambridge, USA

⁶Ladybug Tools LLC, Boston, USA

⁷Kieran Timberlake Research Group, Philadelphia, USA

Correspondence: Amir A. Aliabadi (aliabadi@uoguelph.ca)

Abstract. The Vertical City Weather Generator (VCWG) is a computationally efficient urban microclimate model developed to predict temporal and vertical variation of potential temperature, wind speed, specific humidity, and turbulence kinetic energy. It is composed of various sub-models: a rural model, an urban vertical diffusion model, a radiation model, and a building energy model. Forced with weather data in a nearby rural site, the rural model is used to solve for the vertical profiles of potential temperature, specific humidity, and friction velocity at 10 m elevation. The rural model also calculates a horizontal pressure gradient. The rural model outputs are applied on a vertical diffusion urban microclimate model that solves vertical transport equations for energy (temperature), momentum, specific humidity, and turbulence kinetic energy. The urban vertical diffusion model is also coupled to the radiation and building energy models using two-way interaction. The aerodynamic and thermal effects of urban elements and vegetation are considered. The predictions of the VCWG model are compared to observations of the Basel UrBan Boundary Layer Experiment (BUBBLE) microclimate field campaign for two weeks starting 21 June 2002. The model evaluation indicates that the VCWG predicts vertical profiles of meteorological variables in reasonable agreement with field measurements. The average BIAS and RMSE for wind speed, temperature, and specific humidity are -0.20 ± 0.50 ms^{-1} , $+0.11 \pm 1.73$ K, and $+0.0011 \pm 0.0016$ kgkg^{-1} , respectively. VCWG-predicted mean and standard deviation for Urban Heat Island (UHI) are $+1.59$ and 1.46 K, respectively, in reasonable agreement with observations reporting a mean and standard deviation for UHI of $+1.72$ and 0.91 K, respectively. The performance of the model is further explored to investigate the effects of urban configurations such as plan and frontal area densities, varying levels of vegetation, building energy configuration, radiation configuration, seasonal variations, and different climate zones on the model predictions. The results obtained from the explorations are reasonably consistent with previous studies in the literature, justifying the reliability and computational efficiency of VCWG for operational urban development projects.

1 Introduction

Urban areas interact with the atmosphere through various exchange processes of heat, momentum, and mass, which substantially impact the human comfort, air quality, and energy consumption. Such complex interactions are observable from the Urban Canopy Layer (UCL) to a few hundred meters within the Atmospheric Boundary Layer (ABL) (Britter and Hanna, 5 2003). Modeling enables a deeper understanding of interactions between urban areas and the atmosphere and can possibly offer solutions toward mitigating adverse effects of urban development on the climate. A brief review of modeling efforts is essential toward more accurate model development for the understanding of urban areas-atmosphere interactions.

Mesoscale models incorporating the urban climate were initially aimed to resolve weather features with grid resolutions of at best few hundred meters horizontally and a few meters vertically, without the functionality to resolve microscale three- 10 dimensional flows or to account for atmospheric interactions with specific urban elements such as roads, roofs, and walls (Bornstein, 1975). These models usually consider the effect of built-up areas by introducing an urban aerodynamic roughness length (Grimmond and Oke, 1999) or adding source or sink terms in the momentum (drag) and energy (anthropogenic heat) equations (Dupont et al., 2004). Therefore, if higher grid resolutions less than ten meters (horizontal and vertical) are desired (Moeng et al., 2007; Wang et al., 2009; Talbot et al., 2012), microscale climate models should be deployed. Some efforts also 15 have begun to develop multiscale climate models by coupling mesoscale and microscale models (Chen et al., 2011; Kochanski et al., 2015; Mauree et al., 2018). Numerous studies have used Computational Fluid Dynamics (CFD) to investigate the urban microclimate taking into account interactions between the atmosphere and the urban elements with full three-dimensional flow analysis (Saneinejad et al., 2012; Blocken, 2015; Nazarian and Kleissl, 2016; Aliabadi et al., 2017; Nazarian et al., 2018). Despite accurate predictions, CFD models are not computationally efficient, particularly for weather forecasting at 20 larger scales and for a long period of time, and they usually do not represent many processes in the real atmosphere such as clouds and precipitation. As an alternative, Urban Canopy Models (UCMs) require understanding of the interactions between the atmosphere and urban elements to parameterize various exchange processes of radiation, momentum, heat, and moisture within and just above the canopy, based on experimental data (Masson, 2000; Kusaka et al., 2001; Chin et al., 2005; Aliabadi et al., 2019), three-dimensional simulations, or simplified urban configurations (Martilli et al., 2002; Krayenhoff et al., 2014, 25 2015; Nazarian and Kleissl, 2016). These urban canopy models are more computationally efficient than CFD models. They are designed to provide more details on heat storage and radiation exchange, while they employ less detailed flow calculations.

Urban microclimate models must account for a few unique features of the urban environment. Urban obstacles such as trees and buildings contribute substantially to the changing of flow and turbulence patterns in cities (Kastner-Klein et al., 2004). Difficulties arise when the spatially inhomogeneous urban areas create highly three-dimensional wind patterns that result in 30 the difficulty of parameterizations (Roth, 2000; Resler et al., 2017). For example, the surfaces of urban obstacles exert form and skin drag and consequently alter flow direction and produce eddies at different spatiotemporal scales. This can lead to the formation of shear layers at roof level with variable oscillation frequencies (Tseng et al., 2006; Masson et al., 2008; Zajic et al., 2011), all of such phenomena should be properly approximated in parameterizations.

Heat exchanges between the indoor and outdoor environments significantly influence the urban microclimate. Various studies have attempted to parametrize heat sources and sinks caused by buildings such as heat fluxes due to infiltration, exfiltration, ventilation, walls, roofs, roads, windows, and building energy systems (Kikegawa et al., 2003; Salamanca et al., 2010; Yaghoobian and Kleissl, 2012). Therefore, a Building Energy Model (BEM) is required to be properly integrated in an urban microclimate model to take account of the impact of building energy performance on the urban microclimate (Bueno et al., 2011, 2012b; Gros et al., 2014). This two-way interaction between the urban microclimate and indoor environment can significantly affect Urban Heat Island (UHI) [K] and energy consumption of buildings (Salamanca et al., 2014).

Urban vegetation can substantially reduce the adverse effects of UHI [K], particularly during heat waves, resulting in more thermal comfort (Grimmond et al., 1996; Akbari et al., 2001; Armson et al., 2012). Urban trees can potentially provide shade and shelter, and therefore, change the energy balance of the individual buildings as well as the entire city (Akbari et al., 2001). A study of the local-scale surface energy balance revealed that the amount of energy dissipated due to the cooling effect of trees is not negligible and should be parameterized properly (Grimmond et al., 1996). In addition, the interaction between urban elements, most importantly trees and buildings, is evident in radiation trapping within the canyon and most importantly shading impact of trees (Krayenhoff et al., 2014; Redon et al., 2017; Broadbent et al., 2019). Buildings and trees obstruct the sky with implications in long and shortwave radiation fluxes downward and upward that may create unpredictable diurnal and seasonal changes in UHI [K] (Kleerekoper et al., 2012; Yang and Li, 2015). Also, it has been shown that not only trees but also the fractional vegetation coverage on urban surfaces can alter urban temperatures with implications in UHI [K] (Armson et al., 2012). Trees, particularly those which are shorter than buildings, also exert drag and alter flow patterns within the canopy, however, this effect is not as significant as that drag induced by buildings (Krayenhoff et al., 2015). Such complex interactions must be accounted for in successful urban microclimate models.

1.1 Research Gaps

Numerous studies have focused on high fidelity urban microclimate models with high spatiotemporal flow resolution, capturing important features of the urban microclimate with acceptable accuracy (Gowardhan et al., 2011; Soulhac et al., 2011; Blocken, 2015; Nazarian et al., 2018). Some example Computational Fluid Dynamics (CFD) models of this kind include Open-source Field Operation And Manipulation (OpenFOAM) (Aliabadi et al., 2017, 2018), Parallelized Large-Eddy Simulation Model (PALM) (Maronga et al., 2015; Resler et al., 2017), and ENVI-met (Crank et al., 2018). Despite the advances, however, high fidelity models capable of resolving three-dimensional flows at microscale are not computationally efficient and they are complex to implement for operational applications. As a remedy, lower-dimensional flow urban microclimate models have been developed with many practical applications in city planning, architecture, and engineering consulting. For example, such bulk flow (single-layer) models as Urban Weather Generator (UWG) calculate the flow dynamics in one point, usually the centre of a hypothetical urban canyon, which is representative of all locations (Mills, 1997; Kusaka et al., 2001; Salamanca et al., 2010; Ryu et al., 2011; Bueno et al., 2012a, 2014). Another bulk flow (single-layer) model is Canyon Air Temperature (CAT) model, which utilizes standard data from a meteorological station to estimate air temperature in a street canyon (Erell and Williamson, 2006). The Town Energy Balance (TEB) calculates energy balances for urban surfaces, which is forced by meteorological

data and incoming solar radiation in the urban site with no connection to rural meteorological conditions (Masson et al., 2002). The Temperatures of Urban Facets - 3D (TUF-3D) model calculates urban surface temperatures with the main focus on three-dimensional radiation exchange, but it adopts bulk flow (single-layer) modeling without a connection to the surrounding rural area (Krayenhoff and Voogt, 2007). More recently TUF-3D was coupled to an Indoor-Outdoor Building Energy Simulator (TUF-3D-IOBES), but still this model adopted a bulk flow (single-layer) parameterization (Yaghoobian and Kleissl, 2012). The multi-layer Building Effect Parametrization-Tree (BEP-Tree) model includes variable building heights, the vertical variation of climate variables and the effects of trees, but it is not linked to a building energy model (Martilli et al., 2002; Krayenhoff, 2014; Krayenhoff et al., 2020). More recently, the BEP model has been coupled to a Building Energy Model (BEP+BEM) but it is forced with meteorological variables from higher altitudes above a city using mesoscale models, instead of near surface meteorological variables measured outside the city (rural areas). An overview of the literature reveals an apparent paucity of an independent urban microclimate model that accounts for some spatiotemporal variation of meteorological parameters in the urban environment and considers the effects of trees, building energy, radiation, and the connection to the near-surface rural meteorological conditions measured outside a city, without the need for mesoscale modeling, computationally efficiently and is operationally simple for practical applications.

1.2 Objectives

In this study, we present a new urban microclimate model, called the Vertical City Weather Generator (VCWG), which attempts to overcome some of the limitations mentioned in the previous section. It resolves vertical profiles of climate variables, such as temperature, wind, and specific humidity, in relation to urban design parameters. VCWG also includes a building energy model. It allows parametric investigation of design options on urban climate control at multiple heights, particularly if multi-storey building design options are considered. This is a significant advantage over the bulk flow (single-layer) models such as UWG, which only consider one point for flow dynamics inside a hypothetical canyon (Masson, 2000; Kusaka et al., 2001; Dupont et al., 2004; Krayenhoff and Voogt, 2007; Lee and Park, 2008; Bueno et al., 2012a, 2014). The VCWG is designed to cycle through different atmospheric stability conditions that could be observed over the course of a day, but it is very computationally efficient with the capability to be run up to and beyond an entire year. The advantages of VCWG are as follows. 1) It does not need to be coupled to a mesoscale weather model because it functions standalone as a microclimate model. 2) Unlike many UCMs that are forced with climate variables above the urban roughness sublayer (e.g. TUF-3D), VCWG is forced with rural climate variables measured at 2 m (temperature and humidity) and 10 m (wind) elevation that are widely accessible and available around the world, making VCWG highly practical for urban design investigations in different climates. Further, unlike UWG, VCWG uses the Monin-Obukhov similarity theory in the rural area to consider effects of thermal stability and aerodynamic roughness length to establish vertical profiles of potential temperature and specific humidity. 3) VCWG provides urban climate information in one dimension, i.e. resolved vertically, which is advantageous over bulk flow (single-layer) models. 4) VCWG is coupled with the building energy model using two-way interaction. 5) Unlike UWG, VCWG considers the effect of trees in the urban climate by modelling evapotranspiration (latent heat transfer), sensible heat transfer, radiation transfer, drag, and other processes due to trees.

To evaluate the model, VCWG's predictions are compared to observation of the Basel UrBan Boundary Layer Experiment (BUBBLE) microclimate field campaign for two weeks starting 21 June 2002 (Christen and Vogt, 2004; Rotach et al., 2005). The model predictions of air temperature, wind speed, and specific humidity are compared to the observations. To explore the model, the VCWG is set to run to investigate the effects of building dimensions, urban vegetation, building energy configuration, radiation configuration, seasonal variations, and other climates.

1.3 Organization of the Article

The paper is structured as follows. Section 2 describes the methodology. In Sect. 2.1, all components of the VCWG and the way that they are integrated are presented. First, the Energy Plus Weather (EPW) dataset is introduced, which is the background rural weather data used to force VCWG. Next, the Rural Model (RM), used to determine the potential temperature profile, specific humidity profile, friction velocity, and the horizontal pressure gradient in the rural area, is described. Then, details are discussed for the one-dimensional vertical diffusion model for the urban environment, the building energy model, and the radiation model, which are forced by the RM to predict the vertical profiles of meteorological quantities in the urban area. Section 2.2 describes the location and details of the BUBBLE field campaign. Section 3 provides the results and discussion. It starts with the detailed evaluation of VCWG by comparing simulation results with those of the BUBBLE field measurements in Sect. 3.1. Then, results from other explorations including effects of building dimensions, foliage density, building energy configuration, radiation configuration, seasonal variation, and different climate zones on urban climate are presented in Sect. 3.2 with limited evaluations against observed UHI [K] values. Finally, Sect. 4 is devoted to conclusions and future work. Additional information about the sub-models and equations used are provided in the appendix.

2 Methodology

2.1 Vertical City Weather Generator (VCWG)

Figure 1 shows the VCWG model schematic. VCWG consists of four integrated sub-models: 1) a Rural Model (RM) (Sect. 2.1.2) forces meteorological boundary conditions on VCWG based on Monin-Obukhov similarity theory (Paulson, 1970; Businger et al., 1971; Dyer, 1974) and a soil energy balance model (Bueno et al., 2012a, 2014); 2) a one-dimensional vertical diffusion model (Sect. 2.1.3) is used for calculation of the vertical profiles of urban microclimate variables including potential temperature, wind speed, specific humidity, and turbulence kinetic energy, considering the effect of trees, buildings, and building energy system. This model was initially developed by Santiago and Martilli (2010) and Simón-Moral et al. (2017), while it was later ingested into another model called the Building Effect Parametrization with Trees (BEP-Tree), considering the effects of trees (Krayenhoff, 2014; Krayenhoff et al., 2015, 2020); 3) a Building Energy Model (BEM) (Sect. 2.1.4) is used to determine the waste heat of buildings imposed on the urban environment. This model is a component of the Urban Weather Generator (UWG) model (Bueno et al., 2012a, 2014); 4) a radiation model with vegetation (Sect. 2.1.5) is used to compute the

longwave and shortwave heat exchanges between the urban canyon, trees, and the atmosphere/sky. A summary of this model is provided by Meili et al. (2020) and references within.

The sub-models are integrated to predict vertical variation of urban microclimate variables including potential temperature, wind speed, specific humidity, and turbulence kinetic energy as influenced by aerodynamic and thermal effects of urban elements including longwave and shortwave radiation exchanges, sensible heat fluxes released from urban elements, cooling effect of trees, and the induced drag by urban obstacles. The RM takes latitude, longitude, dry bulb temperature, relative humidity, dew point temperature, and pressure at 2 m elevation, wind speed and direction at 10 m elevation, down-welling direct shortwave radiation, down-welling diffuse shortwave radiation, down-welling longwave radiation, and deep soil temperature from an EPW file. For every time step, and forced with the set of weather data, the RM then computes a potential temperature profile, a specific humidity profile, friction velocity, and a horizontal pressure gradient as a function of friction velocity, all of which are forced as boundary conditions to the one-dimensional vertical diffusion model in the urban area. The potential temperature and specific humidity are forced as fixed values on top of the domain for the urban vertical diffusion model in the temperature and specific humidity equations, respectively. The horizontal pressure gradient is forced as a source term for the urban vertical diffusion model in the momentum equation. While forced by the RM, the urban one-dimensional vertical diffusion model is also coupled with the building energy and radiation models. The three models have feedback interaction. The urban one-dimensional vertical diffusion model calculates the flow quantities at the centre of control volumes, which are generated by splitting the urban computational domain into multiple layers within and above the urban canyon (see Fig. 2). The urban domain extends to three times building height that conservatively falls closer to the top of the atmospheric roughness sublayer in the urban area (Santiago and Martilli, 2010; Aliabadi et al., 2017), but within the inertial layer in the rural area, where Monin-Obukhov similarity theory can be applied (Basu and Lacser, 2017). The feedback interaction coupling scheme among the building energy model, radiation model, and the urban one-dimensional vertical diffusion model is designed to update the boundary conditions, surface temperatures, and the source/sink terms in the transport equations in successive time step iterations. More details about the sub-models are provided in the subsequent sections and the appendix.

2.1.1 Energy Plus Weather Data

Building energy and solar radiation simulations are typically carried out with standardized weather files. EPW files include recent weather data for 2100 locations and are saved in the standard EnergyPlus format, developed by US department of energy.¹ The data is available for most North American cities, European cities, and other regions around the World. The weather data are arranged by World Meteorological Organization (WMO) based on region and country. An EPW file contains typical hourly-based data of meteorological variables. The meteorological variables are dry bulb temperature, dew point temperature, relative humidity, incoming direct and diffusive shortwave radiation fluxes from the sky, incoming longwave radiation flux, wind direction, wind speed, sky condition, precipitation (occasionally), deep soil temperature, and general information about field logistics and soil properties. Precipitation data is often missing in the EPW files.

¹<https://energyplus.net/weather>

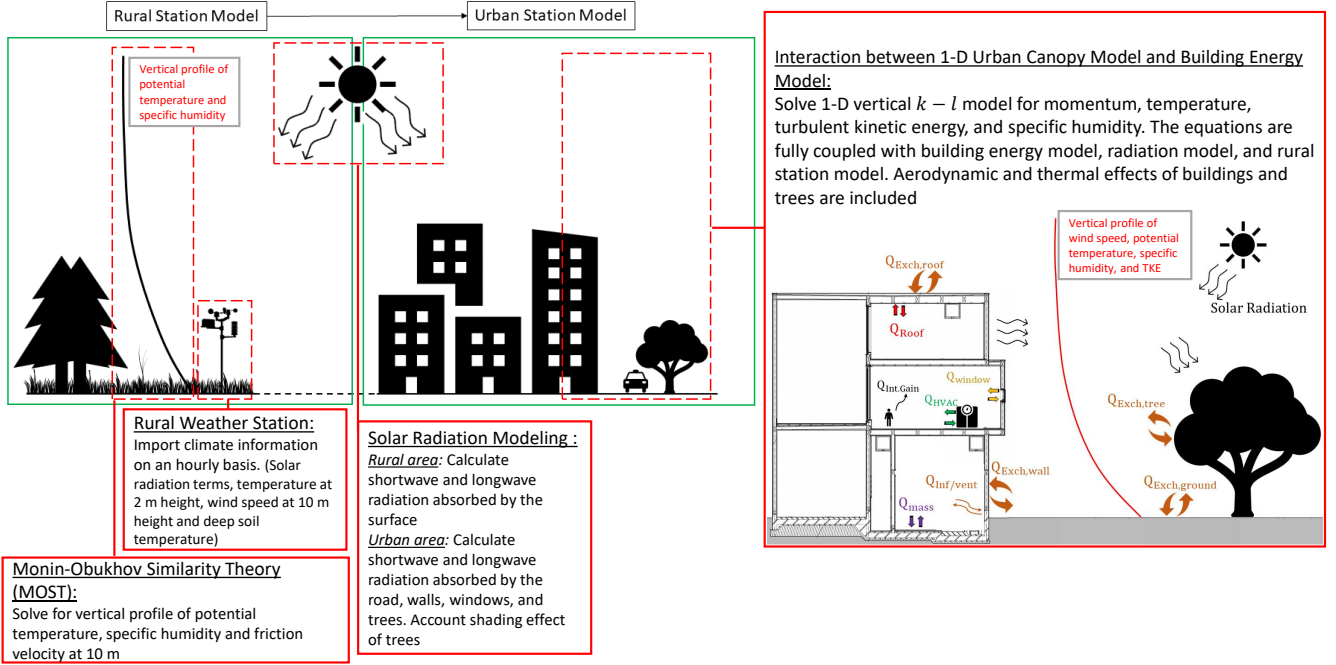


Figure 1. The schematic of Vertical City Weather Generator (VCWG).

2.1.2 Rural Model

In the rural model, the Monin–Obukhov Similarity Theory (MOST) is used to solve for the vertical profiles of potential temperature, specific humidity, and friction velocity at 10 m elevation using meteorological measurements near the surface. MOST is usually applied to the atmospheric surface layer over flat and homogeneous lands to describe the vertical profiles of wind speed, potential temperature, and specific humidity as functions of momentum flux, sensible heat flux, and latent heat flux measured near the surface, respectively. Using MOST the gradient of potential temperature is given by

$$\frac{\partial \bar{\Theta}_{rur}}{\partial z} = \frac{Q_{sen,rur}}{\rho C_p \kappa u_* z} \Phi_H \left(\frac{z}{L} \right), \quad (1)$$

where $\bar{\Theta}_{rur}$ [K] is mean potential temperature in the rural area, $Q_{sen,rur}$ [Wm^{-2}] is net rural sensible heat flux, ρ [kgm^{-3}] is air density near the rural surface, C_p [$Jkg^{-1}K^{-1}$] is air specific heat capacity, u_* [ms^{-1}] is friction velocity, and $\kappa=0.4$ [-] is the von Kármán constant. Φ_H [-] is known as the universal dimensionless temperature gradient. This term is estimated for different thermal stability conditions based on experimental data by (Businger et al., 1971; Dyer, 1974)

$$\Phi_H \left(\frac{z}{L} \right) = \begin{cases} 1 + 5 \frac{z}{L}, & \frac{z}{L} > 0 (\text{Stable}) \\ 1, & \frac{z}{L} = 0 (\text{Neutral}) \\ \left(1 - \frac{16z}{L} \right)^{-1/2}, & \frac{z}{L} < 0 (\text{Unstable}). \end{cases} \quad (2)$$

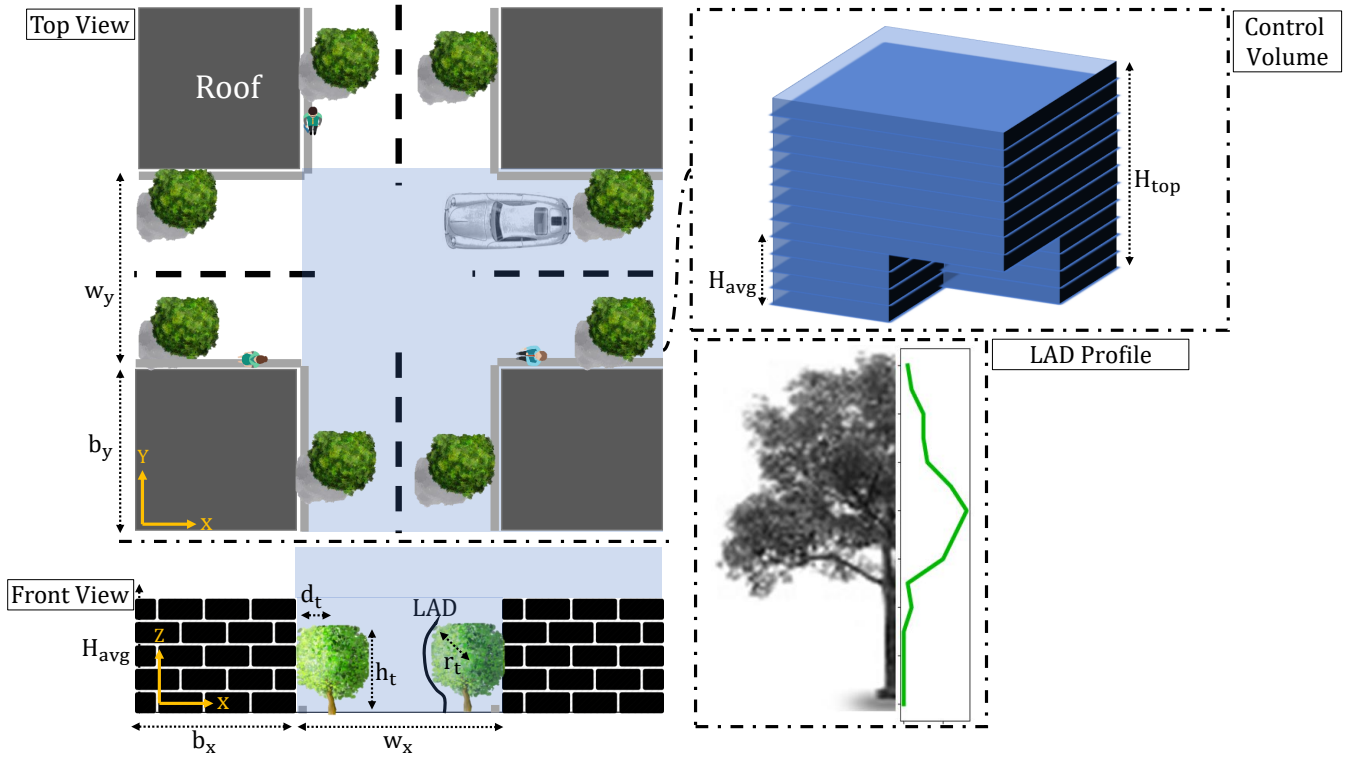


Figure 2. Simplified urban area used in VCWG and corresponding layers of control volumes within and above the canyon. The height of the domain is three times of the average building height. A leaf area density (LAD) [m^2m^{-3}] profile is considered to represent the tree.

In the dimensionless stability parameter z/L [-], z [m] is height above ground and L [m] is Obukhov-Length given by

$$L = \frac{-\bar{\Theta}_{rur, z=2m} u_*^3}{g\kappa \frac{Q_{sen, rur}}{\rho C_p}}. \quad (3)$$

It has been observed that there is a monotonic reduction in friction velocity with increasing stratification (Joffre et al., 2001). So, friction velocity in Eq. 1 is estimated from momentum flux generalization (Monin and Obukhov, 1957)

$$5 \quad \frac{\partial \bar{S}_{rur}}{\partial z} = \frac{u_*}{\kappa z} \Phi_M \left(\frac{z}{L} \right), \quad (4)$$

where \bar{S}_{rur} [ms^{-1}] is the mean horizontal wind speed in the rural area and Φ_M [-] is the universal dimensionless wind shear and is estimated for different thermal stability conditions based on experimental data (Businger et al., 1971; Dyer, 1974)

$$\Phi_M \left(\frac{z}{L} \right) = \begin{cases} 1 + 5 \frac{z}{L}, & \frac{z}{L} > 0 (\text{Stable}) \\ 1, & \frac{z}{L} = 0 (\text{Neutral}) \\ \left(1 - \frac{16z}{L}\right)^{-1/4}, & \frac{z}{L} < 0 (\text{Unstable}). \end{cases} \quad (5)$$

Friction velocity can be determined by integrating Eq. 4 from the elevation of the rural aerodynamic roughness length $z_{0,rur}$ [m] to 10 m in an iterative process. This method provides a friction velocity that is corrected for thermal stability effects. The potential temperature profiles are also obtained by integration of Eq. 1 (Paulson, 1970).

Given the similarity of heat and mass transfer, the same universal dimensionless temperature gradient can be used for the universal dimensionless specific humidity gradient, i.e. $\Phi_Q = \Phi_H$ [-] (Zeng and Dickinson, 1998). The net rural latent heat flux $Q_{lat,rur}$ [Wm^{-2}] can either be directly measured or estimated using the Bowen ratio β_{rur} [-] and the net rural sensible heat flux via $Q_{lat,rur} = Q_{sen,rur} / \beta_{rur}$ [Wm^{-2}]. So the gradient of the specific humidity can be given by the following expression employing latent heat of vaporization L_v [Jkg^{-1}], which can also be integrated to give the vertical profile of specific humidity,

$$10 \quad \frac{\partial \bar{Q}_{rur}}{\partial z} = \frac{Q_{lat,rur}}{\rho L_v \kappa u_* z} \Phi_Q \left(\frac{z}{L} \right). \quad (6)$$

Meteorological information obtained from the weather station including direct and diffuse shortwave radiation, longwave radiation, temperature at 2 m elevation, wind speed at 10 m elevation, and deep soil temperature are used to calculate the net rural sensible and latent heat fluxes at the surface via the surface energy balance

$$Q_{S,rur} + Q_{L,rur} = Q_{sen,rur} + Q_{lat,rur} + Q_{grd}, \quad (7)$$

15 where $Q_{S,rur}$ and $Q_{L,rur}$ are net shortwave and longwave radiation fluxes at the surface (positive with energy flux into the surface) and $Q_{sen,rur}$, $Q_{lat,rur}$, and Q_{grd} [all in Wm^{-2}] are net sensible, latent, and ground heat fluxes at the surface (positive with energy flux leaving the surface). Appendix A details the calculation of each term.

The rural model also outputs a horizontal pressure gradient based on the friction velocity calculation that is later used as a source term for the urban one-dimensional vertical diffusion momentum equation. The pressure gradient is parameterized as $\rho u_*^2 / H_{top}$ [$kgm^{-2}s^{-2}$], where H_{top} [m] is the height of the top of the domain (Krayenhoff et al., 2015; Nazarian et al., 2020), here three times the average building height.

After calculating potential temperature and specific humidity at the top of the domain by the rural model, these values can be applied as fixed-value boundary condition at the top of the domain in the urban one-dimensional vertical diffusion model in the temperature (energy) and specific humidity transport equations.

25 **2.1.3 Urban Vertical Diffusion Model**

Numerous studies have attempted to parameterize the interaction between urban elements and the atmosphere in terms of dynamical and thermal effects, from very simple models based on MOST (Stull, 1988), to the bulk flow (single-layer) parameterizations (Krayenhoff and Voogt, 2007; Masson, 2000; Kusaka et al., 2001; Bueno et al., 2014), to multi-layer models (Hamdi and Masson, 2008; Santiago and Martilli, 2010; Krayenhoff et al., 2015, 2020) with different levels of complexity. The multi-layer models usually treat aerodynamic and thermal effects of urban elements as sink or source terms in temperature (energy), momentum, specific humidity, and turbulence kinetic energy equations. Parameterization of the exchange processes between the urban elements and the atmosphere can be accomplished using either experimental data or CFD simulations (Martilli et al.,

2002; Dupont et al., 2004; Kondo et al., 2005; Kono et al., 2010; Lundquist et al., 2010; Santiago and Martilli, 2010; Krayen-
hoff et al., 2015; Aliabadi et al., 2019). CFD-based parameterizations proposed by Martilli and Santiago (2007), Santiago and
Martilli (2010), Krayenhoff et al. (2015), Nazarian et al. (2020) use results from Reynolds-Averaged Navier-Stokes (RANS)
or Large-Eddy Simulations (LES) including effects of trees and buildings. These parameterizations consider the CFD results
5 at different elevations after being temporally and horizontally averaged.

For the one-dimensional vertical diffusion model, any variable such as cross- and along-canyon wind velocities (U and
 V [ms^{-1}], respectively), potential temperature (Θ [K]), and specific humidity (Q [kgkg^{-1}]) is presented using Reynolds
averaging. The one-dimensional time-averaged momentum equations in the cross- and along-canyon components can be shown
as (Santiago and Martilli, 2010; Krayenhoff, 2014; Krayenhoff et al., 2015; Simón-Moral et al., 2017; Nazarian et al., 2020;
10 Krayenhoff et al., 2020)

$$\frac{\partial \bar{U}}{\partial t} = - \underbrace{\frac{\partial \bar{u}\bar{w}}{\partial z}}_I - \underbrace{\frac{1}{\rho} \frac{\partial \bar{P}}{\partial x}}_{II} - \underbrace{D_x}_{III}, \quad (8)$$

$$\frac{\partial \bar{V}}{\partial t} = - \underbrace{\frac{\partial \bar{v}\bar{w}}{\partial z}}_I - \underbrace{\frac{1}{\rho} \frac{\partial \bar{P}}{\partial y}}_{II} - \underbrace{D_y}_{III}, \quad (9)$$

where \bar{P} [Pa] is time-averaged pressure. The terms on the right hand side of Eqs. 8 and 9 are the vertical gradient of turbulent
flux of momentum (I), acceleration due to the large-scale pressure gradient (II), and the sum of pressure, building form,
15 building skin, and vegetation drag terms (III). The parameterization of the latter term is detailed in Appendix A and is not
reported here for brevity. K-theory is used to parameterize the vertical momentum fluxes, i.e. $\partial \bar{u}\bar{w} / \partial z = -K_m \partial \bar{U} / \partial z$ and
 $\partial \bar{v}\bar{w} / \partial z = -K_m \partial \bar{V} / \partial z$ (the same approach will be used in temperature (energy) and specific humidity equations), where the
diffusion coefficient is calculated using a $k-\ell$ turbulence model

$$K_m = C_k \ell_k k^{1/2}, \quad (10)$$

20 where C_k [-] is a constant and ℓ_k [m] is a length scale optimized using sensitivity analysis based on CFD (Nazarian et al.,
2020). Note that the plan area density λ_p [-] in this study is greater than the limit considered by Nazarian et al. (2020), so
we assume that the parameterizations extrapolate to this value of λ_p [-]. More details on C_k [-] and ℓ_k [m] are provided in
Krayenhoff (2014) and Nazarian et al. (2020). The turbulence kinetic energy k [m^2s^{-2}] can be calculated using a prognostic
equation (Krayenhoff et al., 2015)

$$25 \quad \frac{\partial k}{\partial t} = \underbrace{K_m \left[\left(\frac{\partial \bar{U}}{\partial z} \right)^2 + \left(\frac{\partial \bar{V}}{\partial z} \right)^2 \right]}_I + \underbrace{\frac{\partial}{\partial z} \left(\frac{K_m}{\sigma_k} \frac{\partial k}{\partial z} \right)}_{II} - \underbrace{\frac{g}{\Theta_0} \frac{K_m}{Pr_t} \frac{\partial \bar{\Theta}}{\partial z}}_{III} + \underbrace{S_{wake}}_{IV} - \underbrace{\varepsilon}_{V}, \quad (11)$$

where g [ms^{-2}] is acceleration due to gravity and Θ_0 [K] is a reference potential temperature. The terms on the right hand
side of Eq. 11 are shear production (I), turbulent transport of kinetic energy parameterized based on K-theory (II), buoyant

production/dissipation (III), wake production by urban obstacles and trees (IV), and dissipation (V). Parameterizations of the last two terms are presented in more detail in Appendix A and by Krayenhoff (2014) and are not reported here for brevity. σ_k [-] is turbulent Prandtl number for kinetic energy, which is generally suggested to be $\sigma_k=1$ [-] (Pope, 2000).

To calculate vertical profile of potential temperature in the urban area, the energy transport equation can be derived as

$$5 \quad \frac{\partial \bar{\Theta}}{\partial t} = \underbrace{\frac{\partial}{\partial z} \left(\frac{K_m}{Pr_t} \frac{\partial \bar{\Theta}}{\partial z} \right)}_I + \underbrace{S_{\Theta R} + S_{\Theta G} + S_{\Theta W} + S_{\Theta V} + S_{\Theta A} + S_{\Theta waste}}_{II}, \quad (12)$$

where Pr_t [-] is turbulent Prandtl number, the first term on the right hand side is turbulent transport of heat (I), and the heat sink/source terms (II) correspond to sensible heat exchanges with roof ($S_{\Theta R}$), ground ($S_{\Theta G}$), wall ($S_{\Theta W}$), urban vegetation $S_{\Theta V}$, and radiative divergence $S_{\Theta A}$ [all in Ks^{-1}]. These terms are detailed in appendix A and by Krayenhoff (2014) and are not reported here for brevity. Contribution of the waste heat emissions from building Heating Ventilation and Air Conditioning

10 (HVAC) system $S_{\Theta waste}$ [Ks^{-1}] is parameterized by

$$S_{\Theta waste} = F_{st} \frac{1}{\rho C_p \Delta z} Q_{HVAC}, \quad (13)$$

where Q_{HVAC} [Wm^{-2}] is total sensible waste heat released into the urban atmosphere per building footprint area, F_{st} [-] is the fraction of waste heat released at street level, while the remainder fraction $(1-F_{st})$ [-] is released at roof level, and Δz [m] is grid discretization in the vertical direction. Depending on the type of building, waste heat emissions can be released partially

15 at street level and the rest at roof level, which can be adjusted by changing F_{st} [-] from 0 to 1. For the BUBBLE campaign, it is assumed that all waste heat was released at roof level, which is more typical in most energy-retrofitted mid-rise apartments (Christen and Vogt, 2004; Rotach et al., 2005). Term Q_{HVAC} [Wm^{-2}] is calculated by the building energy model as

$$Q_{HVAC} = \underbrace{(Q_{surf} + Q_{ven} + Q_{inf} + Q_{int})}_{Q_{cool}} + W_{cool} + Q_{dehum} + Q_{gas} + Q_{water}, \quad (14)$$

Cooling waste heat

$$Q_{HVAC} = \underbrace{(Q_{surf} + Q_{ven} + Q_{inf} + Q_{int})}_{Q_{heat}} / \eta_{heat} + Q_{dehum} + Q_{gas} + Q_{water}, \quad (15)$$

Heating waste heat

20 under cooling and heating modes, respectively. Under cooling mode Q_{HVAC} [Wm^{-2}] is calculated by adding the cooling demand (Q_{cool} [Wm^{-2}]), consisting of surface cooling demand, ventilation demand, infiltration (or exfiltration) demand, and internal energy demand (lighting, equipment, and occupants), energy consumption of the cooling system (W_{cool} [Wm^{-2}]) (accounting for Coefficient of Performance (COP [-])), dehumidification demand (Q_{dehum} [Wm^{-2}]), energy consumption by gas combustion (e.g. cooking) (Q_{gas} [Wm^{-2}]), and energy consumption for water heating (Q_{water} [Wm^{-2}]). Under heating

25 mode, Q_{HVAC} [Wm^{-2}] is calculated by adding the heating waste heat (Q_{heat} [Wm^{-2}]), consisting of surface heating demand,

ventilation demand, infiltration (or exfiltration) demand, and internal energy demand (lighting, equipment, and occupants) (accounting for thermal efficiency of the heating system (η_{heat} [-])), dehumidification demand (Q_{dehum} [Wm^{-2}]), energy consumption by gas combustion (e.g. cooking) (Q_{gas} [Wm^{-2}]), and energy consumption for water heating (Q_{water} [Wm^{-2}]).

To complete the urban one-dimensional vertical diffusion model, the transport equation for specific humidity is

$$5 \quad \frac{\partial \bar{Q}}{\partial t} = \underbrace{\frac{\partial}{\partial z} \left(\frac{K_m}{Sc_t} \frac{\partial \bar{Q}}{\partial z} \right)}_I + \underbrace{S_{QV}}_{II}, \quad (16)$$

where \bar{Q} [kgkg^{-1}] is time-averaged specific humidity. The turbulent transport of specific humidity (I) is parameterized based on K-theory, Sc_t [-] is turbulent Schmidt number, and source term S_{QV} [$\text{KgKg}^{-1}\text{s}^{-1}$] (II) is caused by latent heat from vegetation detailed in appendix A and by Krayenhoff (2014) but not reported here for brevity.

2.1.4 Building Energy Model

- 10 In this study, the balance equation for convection, conduction, and radiation heat fluxes is applied to all building elements (wall, roof, floor, windows, ceiling, and internal mass) to calculate the indoor air temperature. Then, a sensible heat balance equation, between convective heat fluxes released from indoor surfaces and internal heat gains and sensible heat fluxes from the HVAC system and infiltration (or exfiltration), is solved to obtain the time evolution of indoor temperature as

$$V \rho C_p \frac{dT_{in}}{dt} = \underbrace{Q_{surf} + Q_{ven} + Q_{inf} + Q_{int}}_{Q_{cool/heat}}, \quad (17)$$

- 15 where V [m^3m^{-2}] is indoor volume per building footprint area, T_{in} [K] is indoor air temperature, and $Q_{cool/heat}$ [Wm^{-2}] is cooling or heating demand as specified in Eqs. 14 and 15. More details on parameterization of the terms in Eq. 17 can be found in appendix A and by Bueno et al. (2012b) but are not reported here for brevity.

- A similar balance equation can be derived for latent heat to determine the time evolution of the indoor air specific humidity as well as the dehumidification load Q_{dehum} [Wm^{-2}], which is parameterized in Bueno et al. (2012b) but is not detailed here for brevity. Note that energy consumption by gas combustion (e.g. cooking) Q_{gas} and water heating Q_{water} [both in [Wm^{-2}]] does not influence indoor air temperature or specific humidity, but such energy consumption sources appear in the waste heat Eqs. 14 and 15. These terms are determined from schedules (Bueno et al., 2012b).

2.1.5 Radiation Model with Vegetation

- In VCWG, there are two types of vegetation: ground vegetation cover and trees. Ground vegetation cover fraction is specified by δ_s [-]. Tree vegetation is specified by four parameters: tree height h_t [m], tree crown radius r_t [m], tree distance from canyon walls d_t [m], and Leaf Area Index (LAI) [m^2m^{-2}], which is the vertical integral of the Leaf Area Density (LAD) [m^2m^{-3}] profile. VCWG considers two trees spaced from the walls of the canyon with distance d_t [m]. Trees cannot be higher than the building height. Both types of vegetation are specified with the same albedo α_V [-] and emissivity ε_V [-]. The VCWG user can change these input parameters for different vegetation structures. The radiation model in VCWG is adapted from the model

developed by Meili et al. (2020). The net all-wave radiation flux is the sum of the net shortwave and longwave radiation fluxes

$$R_n = S^\downarrow - S^\uparrow + L^\downarrow - L^\uparrow, \quad (18)$$

where S^\downarrow , S^\uparrow , L^\downarrow , and L^\uparrow [all in Wm^{-2}] represent the incoming shortwave, outgoing shortwave, incoming longwave, and outgoing longwave radiation fluxes. The incoming shortwave radiation fluxes (direct and diffuse) and the longwave radiation flux from the sky are forced by the EPW file. The absorbed (net) shortwave radiation on surface i is given by

$$S_{n,i} = (1 - \alpha_i) \left(S_i^\downarrow \right) = (1 - \alpha_i) \left(S_i^{\downarrow \text{direct}} + S_i^{\downarrow \text{diffuse}} \right), \quad (19)$$

where α_i is the albedo of the surface and $S_i^{\downarrow \text{direct}}$ and $S_i^{\downarrow \text{diffuse}}$ [Wm^{-2}] are the direct and diffuse incoming shortwave radiation fluxes to surface i . Here i can be S, G, V, W, or T for sky, ground, ground vegetation, wall, and tree. The amount of direct shortwave radiation received by each urban surface is calculated considering shade effects according to well-established methodologies for the case with no trees (Masson, 2000; Kusaka et al., 2001; Wang et al., 2018) and with trees (Ryu et al., 2016). Sky view factors are used to determine the amount of diffuse shortwave radiation that reaches a surface from sky. Infinite reflections of diffuse shortwave radiation are calculated within the urban canyon with the use of view factors for each pair of urban surfaces (Wang, 2010, 2014). The absorbed (net) longwave radiation for each surface is calculated by

$$L_{n,i} = \varepsilon_i \left(L_i^\downarrow - \sigma T_i^4 \right), \quad (20)$$

where ε_i [-] is the emissivity of the surface, $(1 - \varepsilon_i)$ [-] is the reflectivity of the surface, L_i^\downarrow [Wm^{-2}] is the incoming longwave radiation flux, $\sigma = 5.67 \times 10^{-8} \text{ Wm}^{-2}\text{K}^{-4}$ is the Stefan Boltzmann constant, and T_i [K] is the surface temperature. Infinite reflections of longwave radiation within the urban canyon are considered with the use of reciprocal view factors. These view factors are derived analytically for the case with no trees (Masson, 2000; Lee and Park, 2008; Wang et al., 2013). If trees are present, the view factors are calculated with a simplified two-dimensional Monte Carlo ray-tracing algorithm (Wang, 2014; Frank et al., 2016). More details about the radiation model are provided in appendix A and by Meili et al. (2020) but are not reported here for brevity.

2.2 Experimental Field Campaign

To evaluate the model, VCWG's predictions are compared to observation of the Basel UrBan Boundary Layer Experiment (BUBBLE) microclimate field campaign (Christen and Vogt, 2004; Rotach et al., 2005) for two weeks starting 21 June 2002. The model predictions of air temperature, wind speed, and specific humidity are compared to the observations. The urban microclimate field measurements were conducted in Basel, Switzerland, a typical quasi two-dimensional urban canyon (47.55°N and 7.58°E). An EPW file is used to force the VCWG simulations. The rural measurements are conducted at 47.53°N and 7.67°E concurrent with the urban measurements. The average building height for the urban area is $H_{\text{avg}}=14.6$ m, and the plan area density is $\lambda_p=0.54$ [-]. The urban canyon axis is oriented in the northeast-southwest direction with canyon axis angle of $\theta_{\text{can}} = 65^\circ$. The x and y directions are set to be cross- and the along-canyon, respectively. The frontal area density is $\lambda_f=0.37$ [-]. In BUBBLE, wind speed was measured at elevations $z = 3.6, 11.3, 14.7, 17.9, 22.4, \text{ and } 31.7$ m; potential temperature was

measured at elevations $z = 2.6, 13.9, 17.5, 21.5, 25.5,$ and 31.2 m; and relative humidity was measured at elevations $z = 2.6$ and 25.5 m. The dataset provides the measurements averaged every 10 min.

3 Results and Discussion

In this section, the VCWG model results are compared to the microclimate field measurements. We also explored the capability of the model to predict urban climate for investigations of the effects of building dimensions, urban vegetation, building energy configuration, radiation configuration, seasonal variations, and other climates. The simplified urban neighbourhood is depicted in Fig. 2. In VCWG, buildings with uniformly-distributed height, equal width, and equal spacing from one another, represent the urban area. The computational domain height is three times the average building height, which makes it suitable for microclimate analysis (Santiago and Martilli, 2010; Aliabadi et al., 2017). A uniform Cartesian grid with 2 m vertical resolution is used, where buildings are removed from control volumes (see Fig. 2). The flow is assumed to be pressure-driven with the pressure gradient of $\rho u_*^2 / H_{\text{top}}$ [$\text{kgm}^{-2}\text{s}^{-2}$], which is decomposed into the x and y directions based on the wind angle. In this equation, the adjustment for wind angle is made based on canyon orientation and the incoming wind angle at the top of the domain. This pressure gradient is forced as source terms on the momentum Eqs. 8 and 9. The boundary condition for potential temperature and humidity equations (Eqs. 12 and 16) are determined from the rural model (see Fig. 1). Thus, the VCWG is aimed to calculate momentum and energy exchanges for the centre of each cell in the vertical direction based on the boundary conditions obtained from the rural model, the building energy model, and the radiation model.

3.1 Detailed Model-Observation Comparison

The results of the VCWG are now compared to the measured data from the BUBBLE campaign. The input parameters representing the urban area are listed in Table 1. The simulations are run for two weeks starting from 21 June 2002 with the first 24 hours treated as model spin-up period. For such analysis, the run time is approximately 1 min, however it can vary slightly depending on the grid spacing and time step.

To compare VCWG results with measured meteorological variables from the BUBBLE campaign, the hourly BIAS and Root Mean Square Error (RMSE) are calculated over an entire diurnal cycle by considering the model results and measurements over the two-week period. These statistics are calculated for wind speed, potential temperature, and specific humidity at different heights. Also the coefficient of determination R^2 [-] is calculated considering all pairs of model and measurement values at all heights. For the UHI [K] the overall mean and standard deviation are calculated.

The error statistics are shown in Figs. 3 to 5. The average BIAS, RMSE, and R^2 for wind speed are -0.20 ms^{-1} , 0.50 ms^{-1} , and 0.62 , respectively. It can be seen that the hourly BIAS is within 1.0 ms^{-1} at all elevations. The average BIAS, RMSE, and R^2 for temperature are $+0.11 \text{ K}$, 1.73 K , and 0.73 , respectively. The temperature BIAS is improved compared to the predecessor UWG model (-0.6 K (Bueno et al., 2012a)). It can be seen that the hourly BIAS is at maximum at 0600 Local Standard Time (LST). This is due to the limitation of the Monin-Obukhov similarity theory under very calm conditions in the early morning ($u_* < 0.1 \text{ ms}^{-1}$) (Stull, 1988), when a realistic boundary condition for potential temperature cannot be imposed

Table 1. List of input parameters used to run VCWG for model evaluation.

Parameter	Symbol	Value
Latitude °N	lat	47.55
Longitude °E	lon	7.58
Season	-	Summer
Plan area density	λ_p	0.54
Frontal area density	λ_f	0.37
Average buildings height [m]	H_{avg}	14.6
Width of canyon [m]	$w_x=w_y=w$	18.2
Average of leaf area density profile within the canyon [m^2m^{-3}]	LAD	0.25
Tree height [m]	h_t	8
Tree crown radius [m]	r_t	2.5
Tree distance from wall [m]	d_t	3
Ground vegetation cover fraction	δ_s	0
Building type	-	Mid rise apartment
Urban albedos (roof, ground, wall, vegetation)	$\alpha_R, \alpha_G, \alpha_W, \alpha_V$	0.22, 0.1, 0.4, 0.2
Urban emissivities (roof, ground, wall, vegetation)	$\varepsilon_R, \varepsilon_G, \varepsilon_W, \varepsilon_V$	0.95, 0.95, 0.95, 0.95
Rural overall albedo	α_{rur}	0.2
Rural overall emissivity	ε_{rur}	0.95
Rural aerodynamic roughness length [m]	z_{0rur}	0.2
Rural Bown ratio	β_{rur}	0.9
Ground aerodynamic roughness length [m]	z_{0G}	0.02
Roof aerodynamic roughness length [m]	z_{0R}	0.02
Vertical resolution [m]	Δz	2
Time step [s]	Δt	60
Canyon axis orientation °N	θ_{can}	65

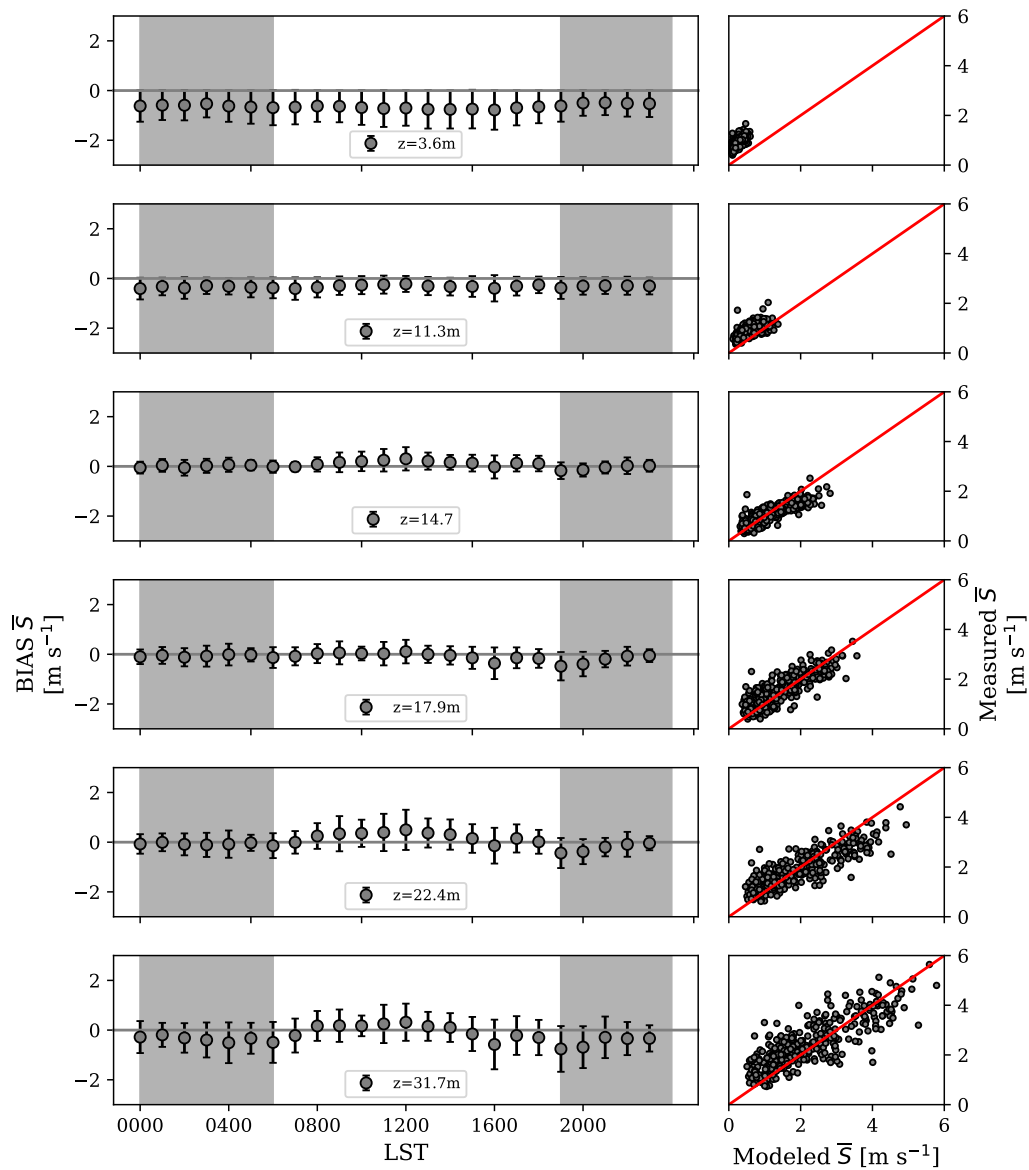


Figure 3. Comparison between the field measurements and the VCWG prediction of wind speed (at various elevations) in the urban site over a two-week period; left) diurnal variation of BIAS and RMSE (error bar); right) scatter plot of modelled versus measured values; nighttime shown with shaded regions; times in Local Standard Time (LST).

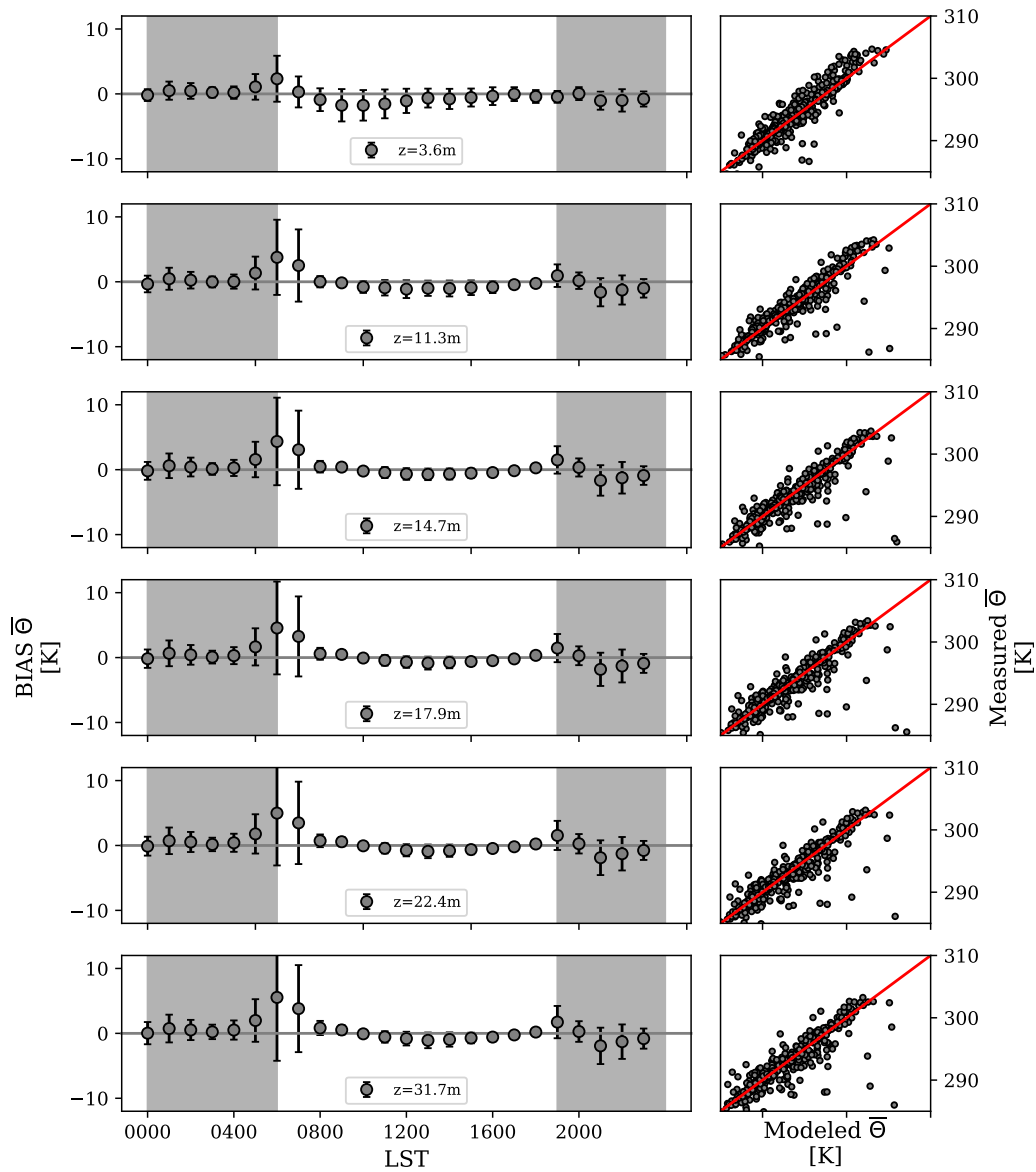


Figure 4. Comparison between the field measurements and the VCWG prediction of potential temperature (at various elevations) in the urban site over a two-week period; left) diurnal variation of BIAS and RMSE (error bar); right) scatter plot of modelled versus measured values; nighttime shown with shaded regions; times in Local Standard Time (LST).

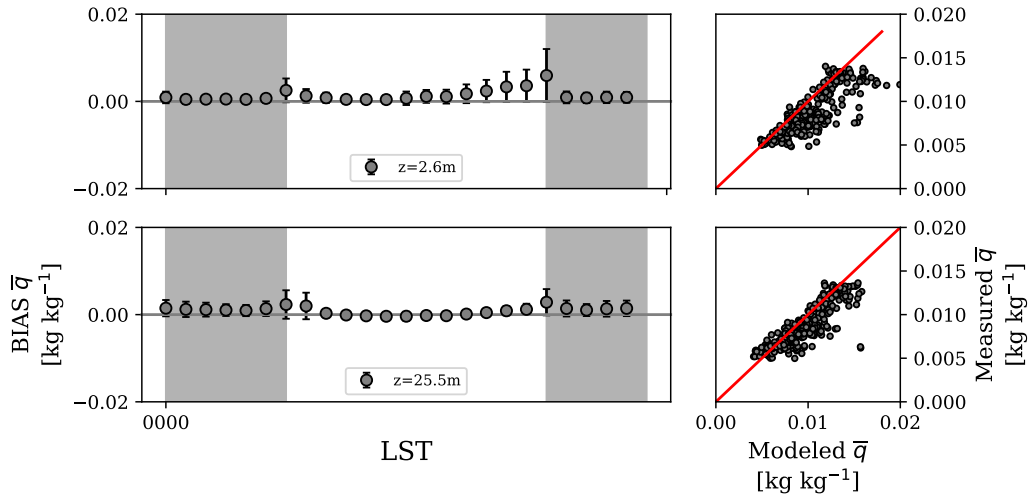


Figure 5. Comparison between the field measurements and the VCWG prediction of specific humidity (at various elevations) in the urban site over a two-week period; left) diurnal variation of BIAS and RMSE (error bar); right) scatter plot of modelled versus measured values; nighttime shown with shaded regions; times in Local Standard Time (LST).

on the top of the domain for the urban vertical diffusion model. This high BIAS is evident on all elevations. The average BIAS, RMSE, and R^2 for specific humidity are $+0.0011 \text{ kgkg}^{-1}$, 0.0016 kgkg^{-1} , and 0.71 , respectively.

UHI [K] for the observation is computed by considering the difference between the temperature measurements inside the canyon at $z = 3.6 \text{ m}$ and those temperatures provided by the EPW dataset. For VCWG, UHI [K] is calculated by considering the difference between the temperature prediction inside the canyon at $z = 3 \text{ m}$ and those temperatures provided by the EPW dataset. Figure 6 shows the diurnal variation of UHI [K] for the field campaign and VCWG. The average VCWG-predicted mean and standard deviation for UHI [K] are $+1.59$ and 1.46 K , respectively. These values are in reasonable agreement with observations reporting mean and standard deviation for UHI of $+1.72$ and 0.91 K , respectively. The average BIAS, RMSE, and R^2 for UHI [K] are -0.14 K , 1.40 K , and 0.51 , respectively.

10 3.2 Model Exploration and Comparison with UHI Observations

The VCWG performance is assessed by evaluating the model performance as a function of the urban configurations ($\lambda_p[-]$, $\lambda_f[-]$, LAD [m^2m^{-3}]), building energy configuration (building type, thermal efficiency, and coefficient of performance), radiation configuration (canyon aspect ratio and axis angle), different seasons, and different climate zones. Except for the analysis of different seasons and climate zones, all explorations are performed by running VCWG to simulate the urban microclimate in Basel, Switzerland, for two weeks starting 21 June 2002, concurrent with the BUBBLE campaign. For exploration of different seasons, VCWG is run to simulate the urban microclimate in Vancouver, Canada, for an entire year in 2011. For different

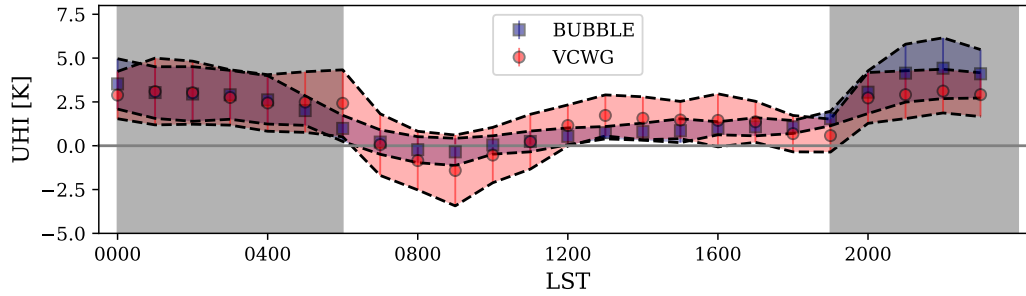


Figure 6. Comparison between the field measurements and the VCWG prediction of UHI [K]; the hourly means and standard deviations (band) are shown; nighttime shown with shaded regions; times in Local Standard Time (LST).

climate zones, VCWG is run to simulate the urban microclimate in other cities for a two-week period. More details on the explorations are provided in the subsequent sections. Such analyses will provide more information on spatiotemporal variation of the atmospheric meteorological variables and reveal the complexity of urban microclimate modeling. Additionally, the potentials and limitations of VCWG will be discussed.

5 3.2.1 Urban Plan and Frontal Area Densities

In urban canopy modeling, two parameters often used to describe building and canyon geometries are plan area density λ_p [-], which is the ratio of the total plan area of the buildings to the total urban flat-earth surface area, and the frontal area density λ_f [-], which is the ratio of the total frontal area (facing wind) to the total urban flat-earth surface area. An urban area can be characterized with different types of land use, where each type may have different plan and frontal area densities, they can vary from high values in industrial and commercial districts to low values associated with the land used for public transportation (Wong et al., 2010). Most development in an urban area could be associated with changing λ_p [-] and λ_f [-], which can alter the local climate in different ways such as air and surface temperatures, building energy consumption, and thermal and wind comfort levels (Coutts et al., 2007; Emmanuel and Steemers, 2018).

Two case studies $\lambda_p=0.46$ and 0.54 [-] (associated with canyon widths of 25 and 18.2 m) are explored to assess the model and see how the urban microclimate changes when the plan area density decreases. Here, except for canyon width, all other model input parameters are kept the same as the evaluation runs. Figure 7 shows typical nighttime and daytime profiles of potential temperature, horizontal wind speed, specific humidity, and turbulence kinetic energy in the urban area associated with running the model for two weeks associated with the BUBBLE field campaign. In this case, higher λ_p [-] is associated with more shading and therefore lower potential temperatures during the day. During the nighttime, the temperature difference between the cases is not as much as the daytime, however, still slightly higher temperatures can be obtained when plan area density is higher. Additionally, more urban surfaces by higher λ_p [-] impose more drag and consequently reduce wind speed

and turbulence kinetic energy during both daytime and nighttime, which can also be depicted in Fig. 8. No change in specific humidity is noted in this exploration.

Further investigations are performed for different frontal area densities $\lambda_f = 0.37$ and 0.51 [-] (associated with building heights 14.6 and 20 m) by running the model for two weeks associated with the BUBBLE field campaign. Here, except for building height, all other model input parameters are kept the same as the evaluation runs. At first glance, the cities with high-rise buildings are supposed to release more heat into the outdoor environment due to greater urban surfaces, but tall buildings can provide solar shading during the daytime and decrease temperature of the surfaces. As shown in Fig. 8, an increase in λ_f [-] reduces potential temperature in the urban area during the day. However, due to the lack of shortwave radiation over nighttime and that urban surfaces are the main source of heat that can be released into the atmosphere, higher λ_f [-] results in higher potential temperatures at nighttime because of longwave radiation trapping. Moreover, increasing frontal area density tends to increase surface roughness and consequently slow down wind speed and reduce the turbulence kinetic energy within the canyon during both daytime and nighttime, which can also be depicted in Fig. 8. No change in specific humidity is noted in this exploration. The VCWG results are also consistent with previous studies in the literature (Coutts et al., 2007; Zajic et al., 2011; Santiago et al., 2014). The findings reported here highlight the careful considerations that need to be accounted for by city planners.

3.2.2 Leaf Area Density

Urban trees interact with the other urban elements by providing shade to reduce temperature of surfaces, removing the stored heat in the canyon substantially, and induce drag to reduce wind speed (Loughner et al., 2012; Krayenhoff et al., 2015; Redon et al., 2017). The capability of VCWG to take into account these effects is assessed by investigating two case studies with LAD [m^2m^{-3}] representing trees with canyon average foliage densities of 0.1 and $0.2 \text{ m}^2\text{m}^{-3}$, respectively, by running the model for two weeks associated with the BUBBLE field campaign. Here, except for LAD [m^2m^{-3}], all other model input parameters are kept the same as the evaluation runs. The result is shown in Fig. 9. The cooling effect of the trees is evident when the average LAD [m^2m^{-3}] of tree foliage increases, resulting in a decrease of potential temperature within the canyon, particularly during the day when the shading effect of trees lowers the surface temperatures and the evapotranspiration of trees lowers the air temperature. Such effects not only can improve thermal comfort at the pedestrian level, but also can reduce the building energy consumption in the Summertime (Souch and Souch, 1993; Akbari et al., 2001). On the other hand, the urban trees are thought to be a sink of momentum and kinetic energy by exerting drag and damping the flow fluctuations (Giometto et al., 2017; Yuan et al., 2017). This effect can also be modeled by VCWG, which predicts slightly lower level of wind speed within the canyon with increasing LAD [m^2m^{-3}]. Increasing LAD [m^2m^{-3}] reduces the turbulence kinetic energy, possibly due to the combined effects of reducing wind speed, LAD [m^2m^{-3}], and the drag coefficient for tree foliage C_{DV} [-], influencing the wake production term S_{wake} [m^2s^{-3}] (Krayenhoff, 2014). Increasing LAD [m^2m^{-3}], however, results in higher levels of specific humidity due to higher evapotranspiration of trees during daytime. The analysis obtained from this exploration is in reasonable agreement with previous works (Souch and Souch, 1993; Loughner et al., 2012; Giometto et al.,

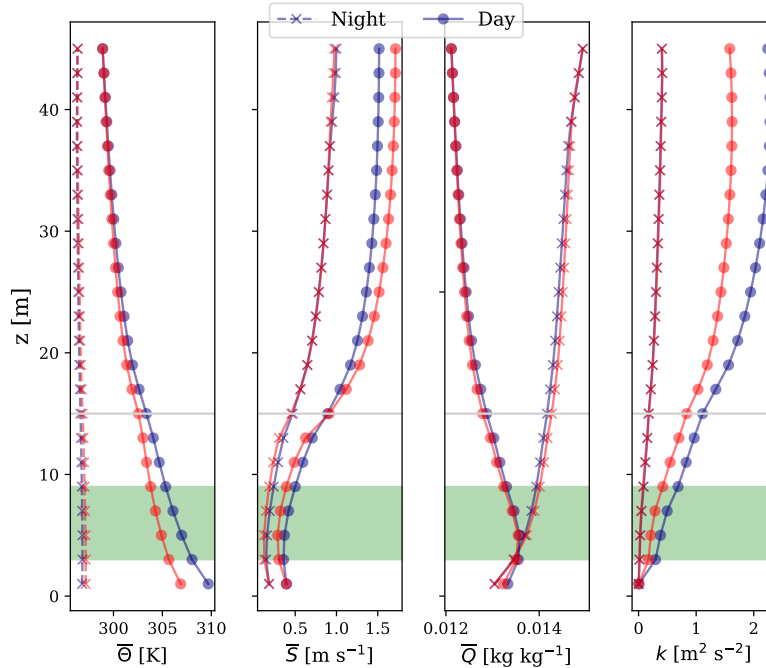


Figure 7. Effect of plan area density λ_p [-] on the profiles of potential temperature, horizontal wind speed, specific humidity, and turbulence kinetic energy during nighttime (averaged from 0000 to 0400 LST) and daytime (averaged from 1200 to 1600 LST); red: $\lambda_p=0.54$ [-], blue: $\lambda_p=0.46$ [-]; tree crown with non-zero LAD [m^2m^{-3}] shown in shaded green; building height shown with grey line; times in Local Standard Time (LST).

2017; Yuan et al., 2017). Trees are recognized to be essential urban elements to moderate extreme wind speeds and heat waves, particularly during the warm season.

3.2.3 Building Energy Configuration

- The building energy model within VCWG is explored by running VCWG under different building types, cooling system
- 5 Coefficient Of Performance (COP) [-], and heating system thermal efficiency η_{heat} [-]. Two building types are considered, the mid-rise apartment and a hospital, with specifications provided in Table 2. It can be noted that the infiltration rate, ventilation rate, volumetric flow for water heating, and waste heat fluxes associated with gas combustion, electricity consumption, and lighting for a hospital are substantially greater than those for a mid-rise apartment. Note that construction material properties are also different among different building types within VCWG schedules, but the differences are not specified here for brevity.
- 10 Two sets of COP [-] and η_{heat} [-] are considered for a mid-rise apartment. For an energy-efficient building default values COP=3.13 [-] and $\eta_{\text{heat}}=0.8$ [-] are used, while for a low-energy-efficient building values COP=1 [-] and $\eta_{\text{heat}}=0.4$ [-]

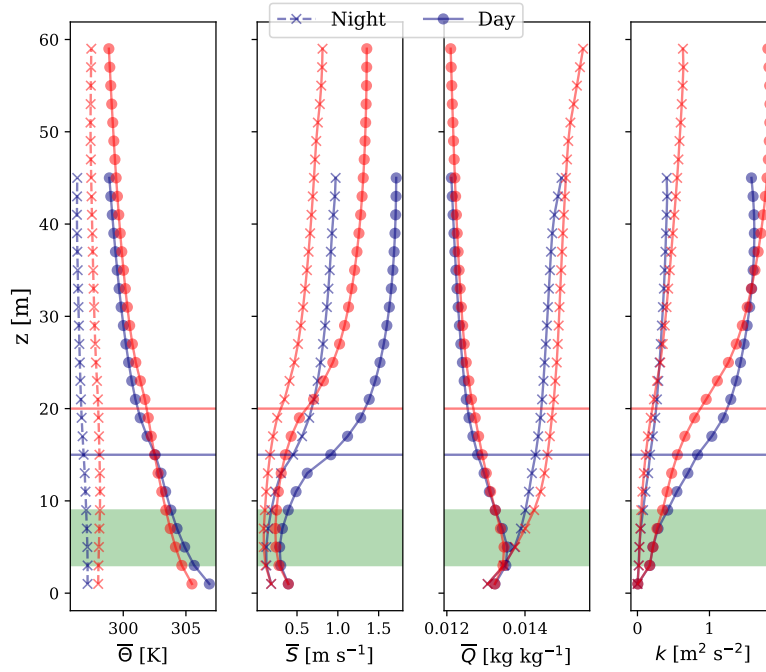


Figure 8. Effect of frontal area density λ_f [-] on the profiles of potential temperature, horizontal wind speed, specific humidity, and turbulence kinetic energy during nighttime (averaged from 0000 to 0400 LST) and daytime (averaged from 1200 to 1600 LST); red: $\lambda_f=0.51$ [-], blue: $\lambda_f=0.37$ [-]; tree crown with non-zero LAD [$\text{m}^2 \text{m}^{-3}$] shown in shaded green; building heights shown with red and blue lines; times in Local Standard Time (LST).

are used. Here, except for building type, COP [-], and η_{heat} [-], all other model input parameters are kept the same as the evaluation runs.

Figure 10 shows the effect of building type on hourly mean and standard deviation of cooling/heating waste heat, dehumidification waste heat, gas combustion waste heat, water heating waste heat, and UHI [K] calculated for running the model for two weeks. The waste heat fluxes are reported per unit building footprint area. It can be noted that the building energy system operates under heating mode for a few hours before sunrise, while it runs under cooling mode for the majority of daytime period. It can be noted that a hospital results in higher values of waste heats and UHI [K], so the potential impact of an energy-intensive hospital on the urban climate may be higher than a mid-rise apartment.

Figure 11 shows the effect of COP [-] and η_{heat} [-] on hourly mean and standard deviation of waste heats and UHI [K] calculated for running the model for two weeks. It can be noted that lower COP [-] and η_{heat} [-] result in higher values of waste heats and slightly higher UHI [K], so the potential impact of an energy-intensive building on the urban climate may be higher than an energy-efficient building. Most particularly, it can be noted that lower heating system thermal efficiency results in greater waste heat flux for water heating.

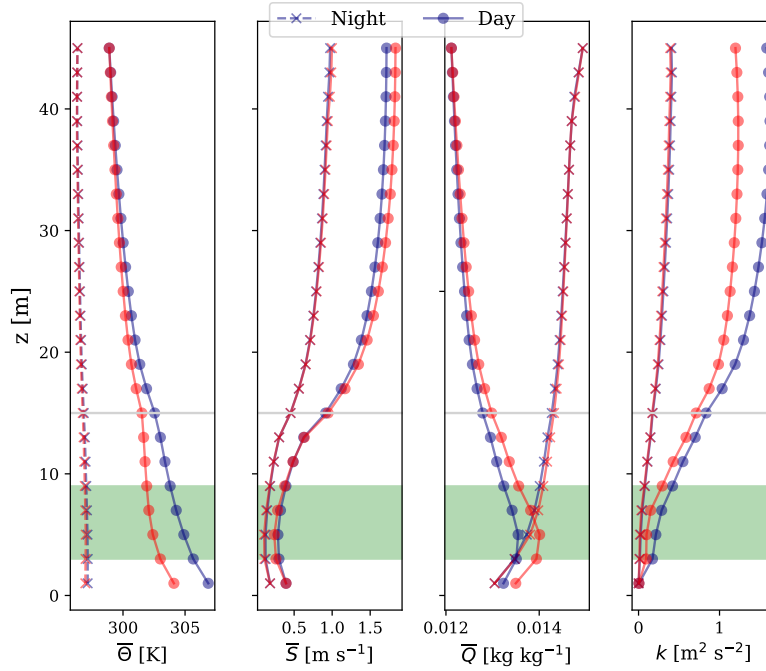


Figure 9. Effect of leaf area density profiles LAD [m^2m^{-3}] on the profiles of potential temperature, horizontal wind speed, specific humidity, and turbulence kinetic energy during nighttime (averaged from 0000 to 0400 LST) and daytime (averaged from 1200 to 1600 LST); red: LAD= $0.2 \text{ m}^2\text{m}^{-3}$, blue: LAD= $0.1 \text{ m}^2\text{m}^{-3}$; tree crown with non-zero LAD [m^2m^{-3}] shown in shaded green; building height shown with grey line; times in Local Standard Time (LST).

Table 2. Specifications of the building energy configuration for two building types. The infiltration is expressed as Air Changes per Hour (ACH [-]).

Building type → Building specification ↓	Mid-rise apartment	Hospital
COP [-]	3.13	5.2
η_{heat} [-]	0.8	0.8
Infiltration (ACH [-])	0.64	0.22
Ventilation [$\text{Ls}^{-1}\text{m}^{-2}$]	0.45	1.8
Average waste heat flux from gas combustion [Wm^{-2}]	0	13
Average waste heat flux from electricity consumption [Wm^{-2}]	5	17
Average waste heat flux from lighting [Wm^{-2}]	5	22

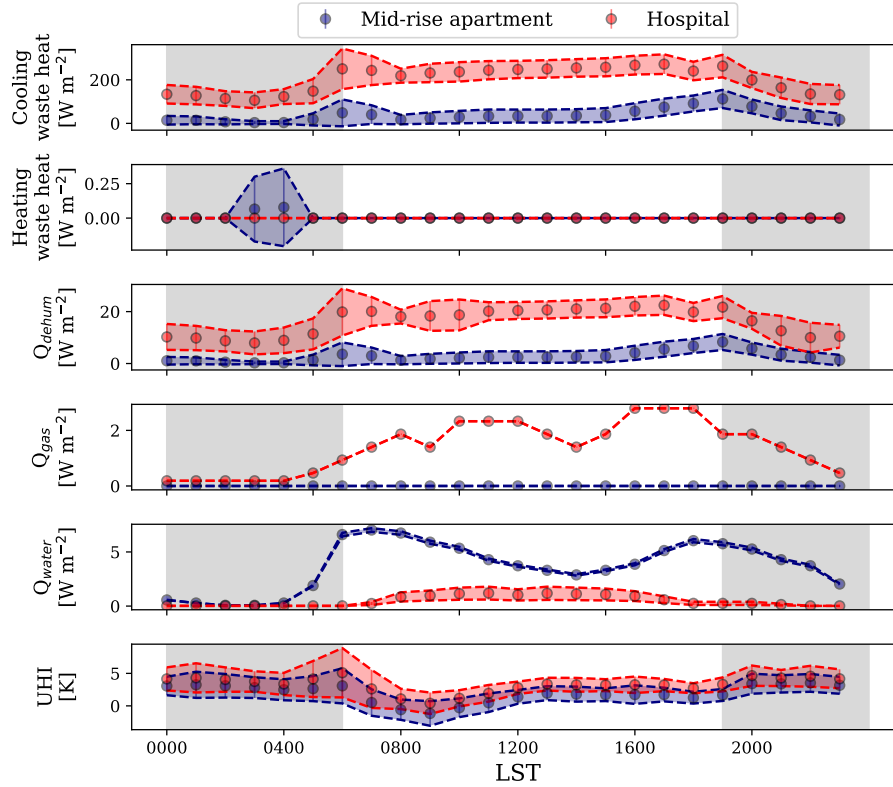


Figure 10. Effect of building type on cooling/heating waste heat, dehumidification waste heat, gas combustion waste heat, water heating waste heat, and UHI [K]; diurnal variation of mean and standard variation (band) are shown using data obtained over a two-week period; nighttime is shown with shaded regions; times in Local Standard Time (LST).

3.2.4 Radiation Configuration

The radiation model within VCWG is explored by running VCWG under different canyon aspect ratios H_{avg}/w [-] and different street canyon axis angles θ_{can} [$^{\circ}$] with respect to the north axis to investigate the effects on shortwave and longwave fluxes. For exploring the effect of canyon aspect ratio on these fluxes, values of $H_{avg}/w=0.8$ and 1.6 [-] are used with keeping $\theta_{can}=0$ $^{\circ}$, while for exploring the effect of street canyon axis angle on these fluxes, values of $\theta_{can}=0$ and 90 $^{\circ}$ with respect to the north axis are used with keeping $H_{avg}/w=0.8$ [-]. For these explorations VCWG is run for two weeks and hourly mean values for radiative fluxes are reported. Here, except for H_{avg}/w [-] and θ_{can} [$^{\circ}$], all other model input parameters are kept the same as the evaluation runs.

Figure 12 shows the shortwave S [Wm^{-2}] and longwave L [Wm^{-2}] radiative fluxes for different canyon aspect ratios. It can be seen that the net shortwave radiation flux, i.e. incoming S^{\downarrow} [Wm^{-2}] minus outgoing S^{\uparrow} [Wm^{-2}] fluxes, by the roof

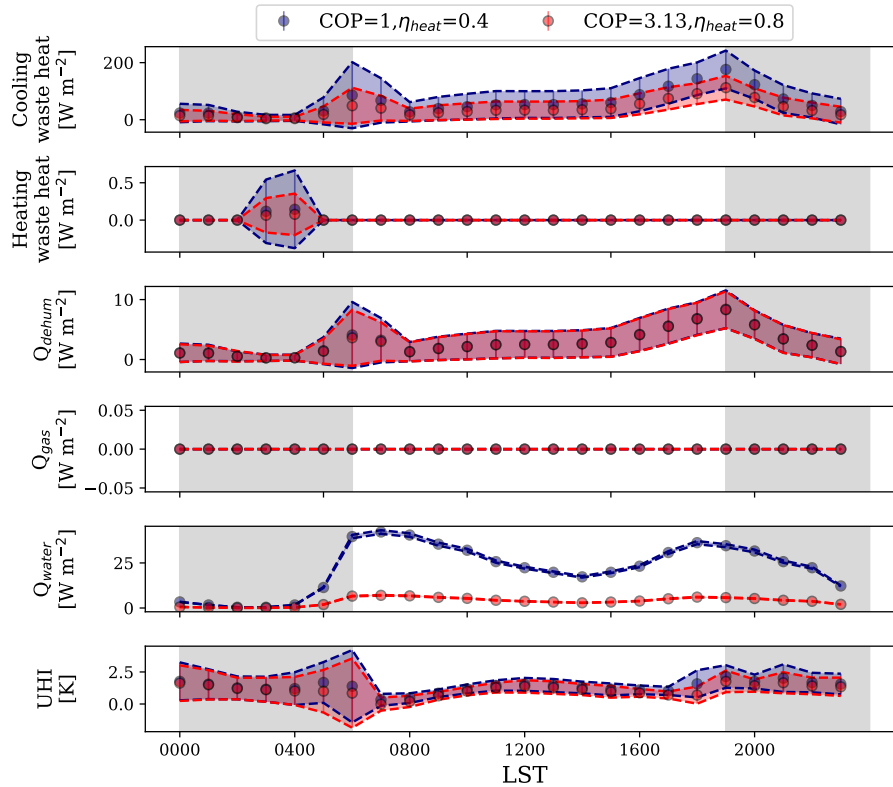


Figure 11. Effect of building cooling system Coefficient Of Performance (COP [-]) and heating system thermal efficiency (η_{heat} [-]) on cooling/heating waste heat, dehumidification waste heat, gas combustion waste heat, water heating waste heat, and UHI [K]; diurnal variation of mean and standard variation (band) are shown using data obtained over a two-week period; nighttime is shown with shaded regions; times in Local Standard Time (LST).

is not affected by the canyon aspect ratio, while the interior surfaces of the urban canyon absorb lower amounts of shortwave radiation fluxes for the higher canyon aspect ratio. This is expected since a higher canyon aspect ratio creates more shading effects on interior canyon surfaces compared to a lower canyon aspect ratio. Focusing on the net shortwave radiation fluxes on the road and tree, it is noted that for the higher aspect ratio canyon the fluxes are more pronounced near noon Local Standard Time (LST), while for the lower aspect ratio canyon the fluxes are pronounced in more hours before and after noon LST. This expected since a higher aspect ratio canyon creates more shading effects on times before and after noon LST compared to a lower aspect ratio canyon. Focusing on the net longwave radiation fluxes, i.e. incoming L^\downarrow [Wm^{-2}] minus outgoing L^\uparrow [Wm^{-2}] fluxes, it is noted that the roof is not affected by the canyon aspect ratio, while the road and wall surfaces of the urban canyon lose lesser amounts of longwave radiation for the higher canyon aspect ratio, both during nighttime and daytime. This can be understood as higher longwave radiation trapping by the higher canyon aspect ratio. For trees, it can be seen that during

daytime, there can be a net longwave radiation gain (as opposed to loss) due to lower vegetation temperatures compared to the surrounding surfaces.

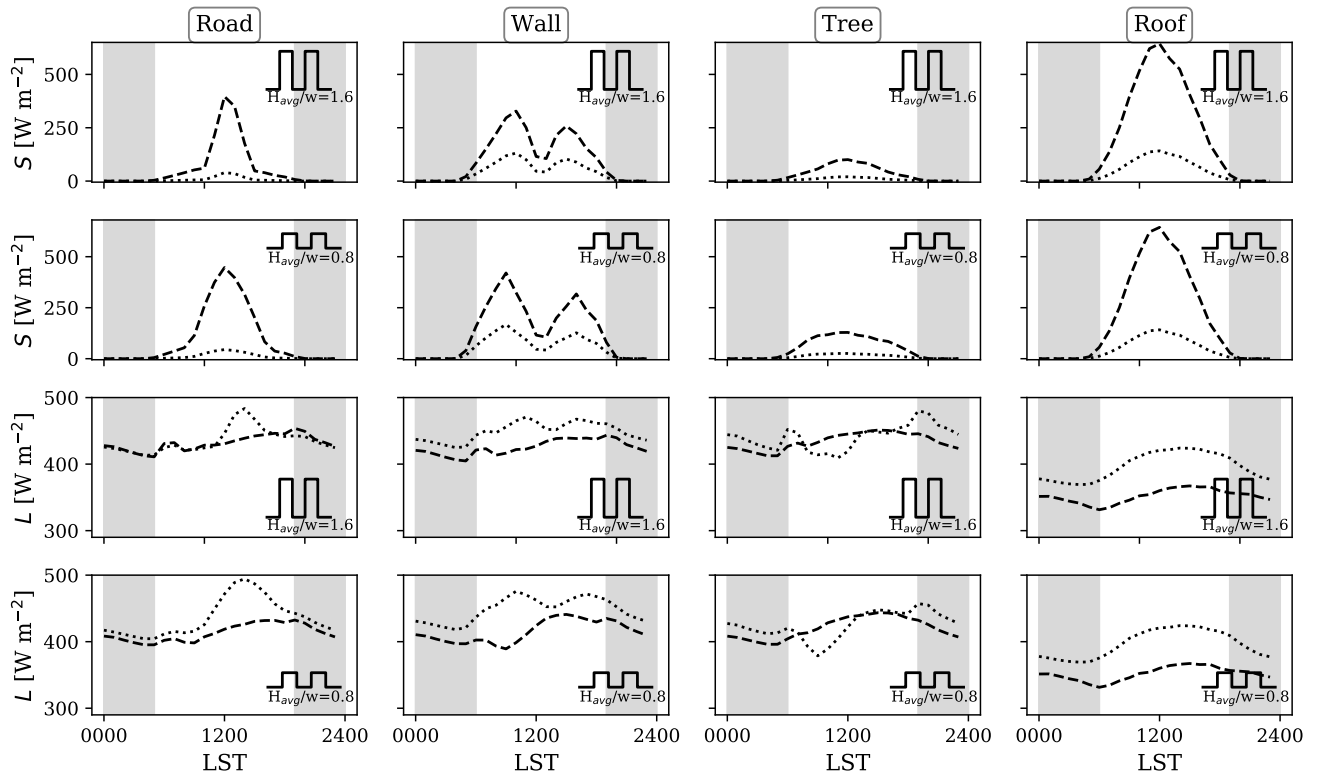


Figure 12. Effect of canyon aspect ratio H_{avg}/w [-] on hourly mean shortwave S [Wm^{-2}] and longwave L [Wm^{-2}] radiation fluxes; incoming fluxes (S^{\downarrow} and L^{\downarrow} [Wm^{-2}]) shown using dashed lines; outgoing fluxes (S^{\uparrow} and L^{\uparrow} [Wm^{-2}]) shown using dotted lines; diurnal variation of mean is shown using data obtained over a two-week period; nighttime is shown with shaded regions; times in Local Standard Time (LST).

Figure 13 shows the radiative fluxes for different street canyon axis angles. It can be seen that the shortwave radiation flux absorbed by the roof is not affected by the street canyon axis angle, while the interior surfaces of the urban canyon show different responses to absorbing the shortwave radiation flux given the street canyon axis angle. With $\theta_{can}=90^{\circ}$ the road surface absorbs the shortwave radiation flux over more hours during the day, given that the combined direct and diffuse shortwave fluxes reach the road surface at both low and high solar zenith and azimuth angles from the east and west directions. On the other hand, with $\theta_{can}=0^{\circ}$ the road surface absorbs the shortwave radiation flux in hours around noon LST, given that this flux reaches the road surface effectively only at low solar zenith and azimuth angles from the north direction. With $\theta_{can}=90^{\circ}$ the wall surface absorbs the shortwave radiation flux in most hours during midday, given that this flux reaches the wall surface with multiple combinations of solar zenith and azimuth angles. On the other hand, with $\theta_{can}=0^{\circ}$ the wall surface

absorbs little shortwave radiation flux in hours around noon LST, given that this flux does not reach the wall surface when the solar azimuth angle is from the north direction. Focusing on the net longwave radiation flux components, the road exhibits a net longwave radiation loss over more prolonged hours of daytime when $\theta_{can}=90^\circ$. The walls exhibit a higher net longwave radiation loss during daytime when $\theta_{can}=0^\circ$. For trees, again, it can be seen that during daytime, there can be a net longwave radiation gain (as opposed to loss) due to lower vegetation temperatures compared to the surrounding surfaces.

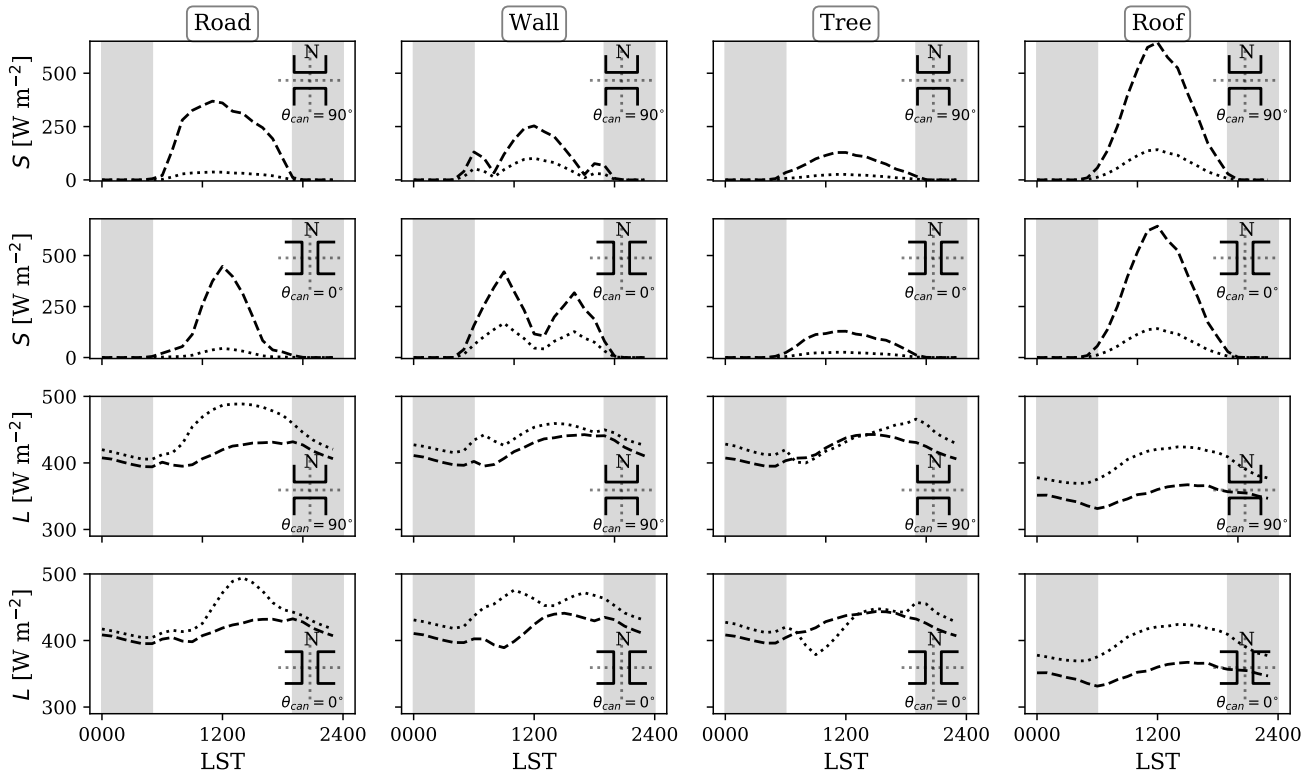


Figure 13. Effect of street canyon axis angle θ_{can} [$^\circ$] on hourly mean shortwave S [Wm^{-2}] and longwave L [Wm^{-2}] radiation fluxes; incoming fluxes (S^\downarrow and L^\downarrow [Wm^{-2}]) shown using dashed lines; outgoing fluxes (S^\uparrow and L^\uparrow [Wm^{-2}]) shown using dotted lines; diurnal variation of mean is shown using data obtained over a two-week period; nighttime is shown with shaded regions; times in Local Standard Time (LST).

3.2.5 Seasonal Variations

In the context of urban development, there are no unique and pre-designed guidelines which can be extended to all built-up areas because careful considerations of geographical features and seasonal variations are required. For example, the type of urban vegetation, which is well suited for both warm and cold seasons in fulfilling thermal and wind comfort standards, can be

climate specific (Jamei et al., 2016). Winter is characterized by larger zenith angles and lower solar radiation fluxes received by the surfaces compared to the other seasons. In Winter, the temperature difference between indoor and outdoor environment is higher than the Summer, thus, seasonal variations can alter building energy consumption and UHI [K] effects substantially (Bueno et al., 2011). In an effort to investigate VCWG's ability to simulate urban climate variables in all seasons, it is run
5 for Vancouver, Canada, for an entire year in 2011. The model input parameters are chosen to correspond to field observations of Runnalls and Oke (2000), in which the urban measurements were in downtown and the rural measurements were 25 km southeast of downtown in the midst of agricultural fields. In this field campaign, the plan area density was $\lambda_p=0.39$ [-], the ratio of total surface to lot area was about 2.2 [-], the canyon angle was $\theta_{can}=-45^\circ$, urban measurement were taken at 10 m elevation, and rural measurements were taken at 2 m elevation. Runnalls and Oke (2000) reported maximum and minimum
10 daily UHI [K] (medians and inner quartiles) for each month of the year.

Figure 14 shows the VCWG results for the hourly mean values of UHI [K] in each month of the year 2011 in Vancouver, Canada. It can be noted that in general early daytime UHI [K] values are lower than nighttime values, as expected. Also the greatest UHI [K] values are noted to occur in August and September. The seasonal variation of UHI [K] as predicted by VCWG is in agreement with a similar map reported by Oke et al. (2017).

15 Figure 15 shows the comparison of VCWG and observed (Runnalls and Oke, 2000) daily maximum and minimum of UHI [K] in each month in Vancouver. The agreement between the model and observations is reasonable. The average BIAS, RMSE, and R^2 for daily maximum and minimum UHI [K] are -0.5 K, 0.45 K, and 0.97 , respectively. It can be seen that the maximum daily UHI [K] can be greater than the minimum daily UHI [K], a phenomenon that the model captures well.

Figure 16 shows the profiles of potential temperature, horizontal wind speed, specific humidity, and turbulence kinetic energy during nighttime (averaged at 0200 LST) and daytime (averaged at 1400 LST) in different seasons for the Vancouver
20 simulation. It is notable that the potential temperature and specific humidity profiles reflect the seasonal patterns (low values in the Winter and high values in the Summer). Wind speed and turbulence kinetic energy profiles do not reveal notable seasonal variations.

3.2.6 Other Climates

25 The VCWG is further explored by predicting UHI [K] in different cities with different climate zones including Buenos Aires in February 1996, a city in the southern hemisphere with hot and humid climate, Vancouver in September 2011, representing a moderate oceanic climate, Osaka in September 1989, with subtropical climate, and Copenhagen in August 1999, representing cold and temperate climate. All simulations are conducted for two weeks and then mean and standard variation of diurnal variations in UHI are calculated (see Fig. 17). Appropriate input parameters for each city are used.

30 The result shows a diurnally-averaged value of $+1.10$ K for UHI [K] for Buenos Aires, which is consistent with a previous study measuring a diurnally-averaged UHI of $+1.3$ K (Bejarán and Camilloni, 2003). In case of Vancouver, the VCWG predicted a diurnally-averaged value of $+1.67$ K for UHI [K] in agreement with a measured daily mean value of $+1.4$ K (Runnalls and Oke, 2000; Lesnikowski, 2014; Ho et al., 2016). Case studies in Japan have reportedly obtained urban warming in large and developed cities such as Osaka, which is the interest in this study, and Tokyo in the afternoon (Leal Filho et al.,

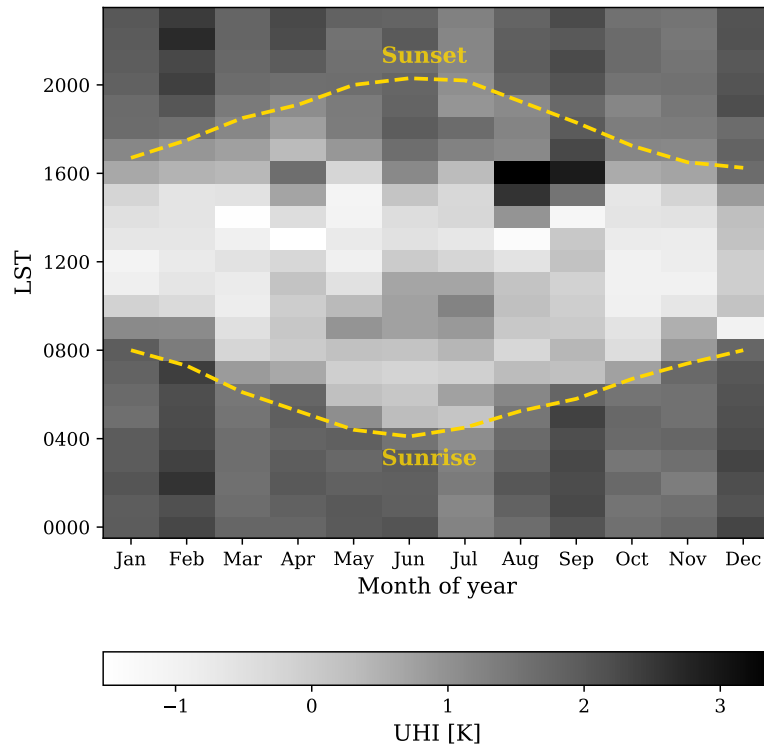


Figure 14. Hourly mean values of UHI [K] in each month in Vancouver, Canada, as predicted by VCWG; sunrise and sunset times are denoted by dashed lines; times in Local Standard Time (LST).

2017). This effect is also predicted by VCWG that showed the diurnally-averaged UHI of +1.78 K, which is consistent with other studies measuring a diurnally-averaged UHI of +1.2 K (Kusaka et al., 2012; Leal Filho et al., 2017). UHI [K] in Copenhagen is reported to change between +0.5 and +1.5 K depending on the wind speed, which agrees reasonably well with the VCWG prediction of UHI [K] varying from a small magnitude during the daytime to large positive values during the night with a diurnal average of +0.75 K (Mahura et al., 2009).

4 Conclusions and Future Work

The Vertical City Weather Generator (VCWG) is an urban microclimate model designed to calculate vertical profiles of meteorological variables including potential temperature, wind speed, specific humidity, and turbulence kinetic energy in an urban area. The VCWG is composed of four sub-models for ingestion of urban parameters and meteorological variables in a rural area (as input and boundary conditions) and prediction of the meteorological variables in a nearby urban area, the building energy performance variables, and the short and longwave radiation transfer processes. VCWG combines elements of several

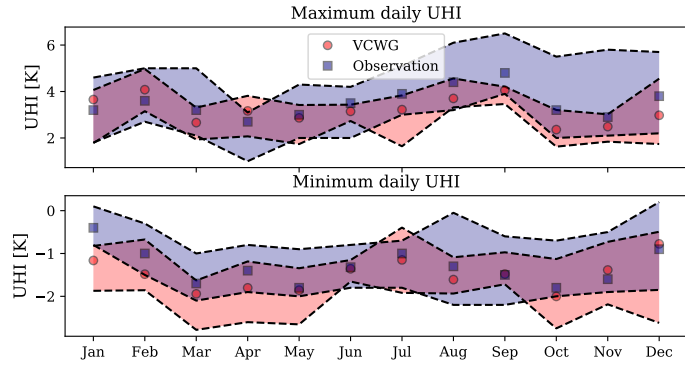


Figure 15. Comparison of VCWG and observed daily maximum and minimum of UHI [K] in each month in Vancouver, Canada; medians are shown with markers and the color bands indicate the inner quartiles; sunrise and sunset times are denoted by dashed lines; observations from Runnalls and Oke (2000).

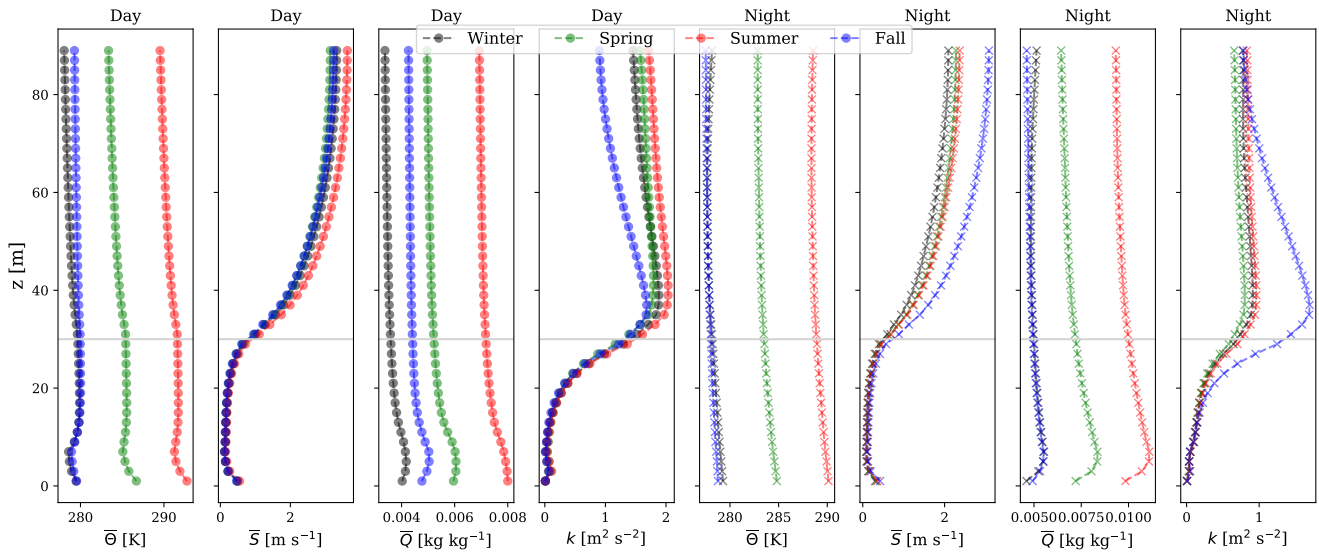


Figure 16. Profiles of potential temperature, horizontal wind speed, specific humidity, and turbulence kinetic energy during nighttime (averaged at 0200 LST) and daytime (averaged at 1400 LST) in different seasons; black: Winter, green: Spring, red: Summer, and blue: Fall; building height shown with grey line; times in Local Standard Time (LST).

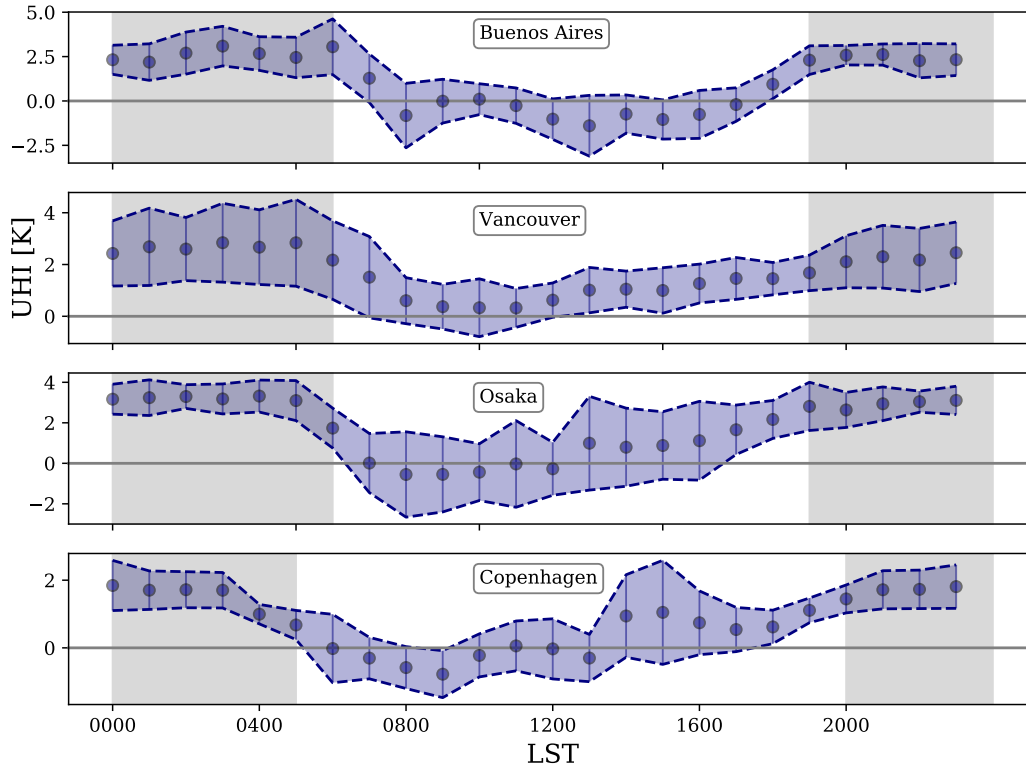


Figure 17. Diurnal variation of the UHI [K] in Buenos Aires, Vancouver, Osaka, and Copenhagen; diurnal variation of mean and standard deviation (band) are shown using data obtained over a two-week period; nighttime is shown with shaded regions; times in Local Standard Time (LST).

previous models developed by Santiago and Martilli (2010), Bueno et al. (2014), Krayenhoff (2014), Krayenhoff et al. (2015), and Meili et al. (2020) to generate a model with the ability to predict vertical profiles of urban meteorological variables, forced by rural measurements, and with two-way coupling with both building energy and radiation models.

To evaluate VCWG, its predictions of potential temperature, wind speed, and specific humidity are compared to observation of the Basel UrBan Boundary Layer Experiment (BUBBLE) microclimate field campaign for two weeks starting 21 June 2002 (Christen and Vogt, 2004; Rotach et al., 2005). The results obtained from VCWG agree reasonably well with the measurements. The average BIAS and RMSE for wind speed, temperature, and specific humidity are $-0.20 \pm 0.50 \text{ ms}^{-1}$, $+0.11 \pm 1.73 \text{ K}$, and $+0.0011 \pm 0.0016 \text{ kgkg}^{-1}$, respectively. The temperature BIAS is improved compared to the predecessor UWG model (-0.6 K (Bueno et al., 2012a)). VCWG-predicted mean and standard deviation for UHI are $+1.59$ and 1.46K , respectively, in reasonable agreement with observations reporting a mean and standard deviation for UHI of $+1.72$ and 0.91 K , respectively.

The performance of the VCWG is further assessed by conducting several types of explorations for both nighttime and daytime urban microclimate. First, we investigate how the urban geometry, which is characterized by plan area density λ_p [-] and frontal area density λ_f [-], can affect the urban microclimate. An increase in λ_p [-] is associated with lower air temperatures (due to shading) and reduces wind speeds within the urban canyon during daytime. A configuration with higher λ_f [-] also increases shading effects and consequently reduces daytime temperatures, but it increases nighttime temperatures due to more heat released from urban surfaces that is trapped in the canyon. The cooling effect of the urban vegetation is also evaluated by changing the Leaf Area Density (LAD [m^2m^{-3}]) profiles within the canyon. Increasing the average LAD [m^2m^{-3}] shows heat removal from the canyon alongside with lower wind speeds due to the drag induced by trees. The VCWG is also run for different building types (a mid-rise apartment and a hospital), cooling system Coefficient of Performance (COP) [-], and heating thermal efficiency (η_{heat} [-]). The results show that a hospital generates more waste heat fluxes associated with cooling and gas consumption, which increase urban temperatures. The analysis of different cooling systems also reveal that less-efficient system (lower COP [-] and η_{heat} [-]) result in more waste heat emission and slightly higher temperatures. The radiation model is assessed by running the VCWG for different canyon aspect ratios and axis angles. The radiation fluxes at the road and walls show differences according to canyon aspect ratio and axis angle, while the fluxes at the tree canopy and roof are less sensitive to the canyon aspect ratio and axis angle. Another exploration made for all months of the year in Vancouver, Canada, justifies the ability of the VCWG to predict the urban microclimate in different seasons. The results show the expected diurnal variation of UHI [K] in the urban site. Also daily maximum and minimum UHI [K] values are in agreement with observations of Runnalls and Oke (2000). The average BIAS and RMSE for daily maximum and minimum UHI [K] are -0.5 K and 0.45 K, respectively. The ability of the model to predict UHI [K] in different cities with different climate zones is assessed. The case studies are Buenos Aires, Vancouver, Osaka, and Copenhagen. All exploration results obtained from the VCWG are reasonably consistent with the previous observations in the literature.

In this study, it is shown that the urban microclimate model VCWG can successfully extend the spatial dimension of the pre-existing bulk flow (single-layer) urban microclimate models to one-dimension in the vertical direction, while it also considers the relationship of the urban microclimate model to the rural meteorological measurements and the building energy conditions. The effect of the key urban elements such as building configuration, building energy systems, and vegetation are considered, but there is still opportunity to improve VCWG further. The urban site is simplified as blocks of buildings with symmetric and regular dimensions, which can be more realistically represented if more considerations are to be taken into account about nonuniform distribution of building dimensions. Future studies can also focus on improvement of flow-field parameterization or including additional source/sink terms in the transport equations to model horizontal motions, eddies, and flow fluctuations in the urban area, which is realistically very three-dimensional and heterogeneous. Urban hydrology can be added to VCWG in the future to account for precipitation effects. At present, the developed VCWG model can account for the spatial variation of urban microclimate in a computationally efficient manner independent of an auxiliary mesoscale model. This advantage is really important for urban planners, architects, and consulting engineers, to run VCWG operationally fast for many projects.

Code and data availability. The VCWG v1.2.0 is developed at the Atmospheric Innovations Research (AIR) Laboratory at the University of Guelph: <http://www.aaa-scientists.com>. The source code is available under GPL 3.0 licence: <https://opensource.org/licenses/GPL-3.0> (last access: May 2019) and can be downloaded from <https://www.zenodo.org/> with DOI: 10.5281/zenodo.3951065.

Appendix A

5 A1 Surface Energy Balance in the Rural Area

In Eq. 7 the net shortwave solar radiation flux absorbed at the surface can be calculated from

$$Q_{S,rur} = ((1 - F_{veg})(1 - \alpha_{rur}) + F_{veg}(1 - \alpha_V))(S^{\downarrow direct} + S^{\downarrow diffuse}), \quad (A1)$$

where F_{veg} [-] is the fraction of the rural area covered by vegetation, α_{rur} [-] is overall albedo of the rural area, α_V [-] is the albedo of vegetation (here considered to be the same for rural and urban vegetation), and $S^{\downarrow direct}$ and $S^{\downarrow diffuse}$ [Wm^{-2}] are the forcing direct and diffuse shortwave radiation fluxes from the EPW file, respectively. The net longwave solar radiation flux absorbed at the surface can be calculated from

$$Q_{L,rur} = L^{\downarrow} - L^{\uparrow} = \varepsilon_{rur} (L^{\downarrow} - \sigma T_{s,rur}^4), \quad (A2)$$

where L^{\downarrow} [Wm^{-2}] is the forcing longwave radiation flux from the EPW file, L^{\uparrow} [Wm^{-2}] is the longwave radiation flux leaving the rural surface at temperature $T_{s,rur}$ [K], and ε_{rur} [-] is rural surface emissivity. The net sensible heat flux is calculated using Louis (1979)

$$Q_{sen,rur} = \rho C_p \frac{\kappa^2}{\left(\ln \frac{z}{z_{0rur}}\right)^2} \frac{1}{R} \bar{S}_{rur,z=10m} (\bar{\Theta}_{rur,s} - \bar{\Theta}_{rur,2m}) F_h \left(\frac{z}{z_{0rur}}, Ri_B \right), \quad (A3)$$

where R [-] is a model constant, Ri_B [-] is the bulk Richardson number, and F_h [-] is the stability function for sensible heat flux defined by Louis (1979). The net latent heat flux is calculated using the Bowen ratio β_{rur} [-] such that $Q_{lat,rur} = Q_{sen,rur} / \beta_{rur}$ [Wm^{-2}]. The ground heat flux drives the conduction equation at the upper most soil layer via (Bueno et al., 2012a)

$$20 \quad dC_v \frac{dT_1}{dt} = C(T_2 - T_1) + Q_{grd}, \quad (A4)$$

where d [m] is the soil layer thickness, C_v [$Jm^{-3}K^{-1}$] is volumetric heat capacity of soil, $T_1 = \bar{\Theta}_{rur,s}$ [k] is soil upper layer temperature (the same as soil surface temperature), C [$Wm^{-2}K^{-1}$] is the soil thermal conductance, and T_2 [K] is soil temperature in the second layer under ground. In the lowest layer (n) of soil the conduction equation is forced by a deep soil temperature T_{deep} [K]

$$25 \quad dC_v \frac{dT_{n-1}}{dt} = C(T_{deep} - T_{n-1}). \quad (A5)$$

A2 Source/Sink Term in the 1-D Model

The pressure and skin drags exerted on the flow in Eqs. 8 and 9 are formulated as follows (Santiago and Martilli, 2010; Krayenhoff, 2014; Krayenhoff et al., 2015; Simón-Moral et al., 2017; Nazarian et al., 2020; Krayenhoff et al., 2020)

$$D_x = \underbrace{\frac{1}{\rho} \frac{\partial \tilde{P}}{\partial x}}_I + \underbrace{\nu(\nabla^2 \tilde{U})}_{II}, \quad (\text{A6})$$

$$5 \quad D_y = \underbrace{\frac{1}{\rho} \frac{\partial \tilde{P}}{\partial y}}_I + \underbrace{\nu(\nabla^2 \tilde{V})}_{II}, \quad (\text{A7})$$

where term I represents dispersive pressure variation (form drag) induced by vegetation and building and term II represents the dispersive viscous dissipation (skin drag) induced by horizontal surfaces. The former can be parameterized as below

$$\frac{1}{\rho} \frac{\partial \tilde{P}}{\partial x} = (B_D C_{DBv} + LAD \Omega C_{DV}) \bar{U}_{expl} \bar{U}, \quad (\text{A8})$$

$$\frac{1}{\rho} \frac{\partial \tilde{P}}{\partial y} = (B_D C_{DBv} + LAD \Omega C_{DV}) \bar{V}_{expl} \bar{V}, \quad (\text{A9})$$

10 where B_D [m^{-1}] is sectional building area density, C_{DBv} [-] is sectional drag coefficient in the presence of trees, LAD [$\text{m}^2 \text{m}^{-3}$] is leaf area density in the canyon, Ω [-] is clumping factor, C_{DV} [-] is the drag coefficient for tree foliage, and \bar{U}_{expl} and \bar{V}_{expl} [ms^{-1}] are wind velocity components in x and y directions from a previous numerical solution, respectively, which are assumed explicitly as constants to linearize the system of equations to be solved. The skin drag can be parameterized as follows

$$15 \quad \nu(\nabla^2 \tilde{U}) = \frac{1}{\Delta z} c_d f_m \bar{U}_{expl} \bar{U}, \quad (\text{A10})$$

$$\nu(\nabla^2 \tilde{V}) = \frac{1}{\Delta z} c_d f_m \bar{V}_{expl} \bar{V}, \quad (\text{A11})$$

where c_d [-] is skin drag coefficient and f_m [-] is a function of stability from Louis (1979).

The terms related to wake production S_{wake} and dissipation rate ε [both in $\text{m}^2 \text{s}^{-3}$] in Eq. 11 can be parameterized as

$$S_{wake} = (B_D C_{DBv} + LAD \Omega C_{DV}) \bar{U}_{expl}^3, \quad (\text{A12})$$

$$20 \quad \varepsilon = C_\varepsilon \frac{k^{\frac{3}{2}}}{\ell_{\varepsilon, dissipation}}, \quad (\text{A13})$$

where Ω [-] is clumping factor, C_ε [-] is a model constant and $\ell_{\varepsilon, dissipation}$ [m] is a dissipation length scale obtained by sensitivity study using CFD (Nazarian et al., 2020). Note that plan area density λ_p [-] in this study is greater than the limit considered by Nazarian et al. (2020), so we assume that the parameterizations extrapolate to this value of λ_p [-].

The heat source/sink terms, terms in Eq. 12, caused by roof ($S_{\Theta R}$) and ground ($S_{\Theta G}$) [both in Ks^{-1}] are calculated based on
25 the study by Louis (1979) and the heat flux from the wall ($S_{\Theta W}$ [Ks^{-1}]) is formulated in Martilli et al. (2002). The two other

source/sink terms can be parameterized as below

$$S_{\Theta A} = \frac{4\rho_{abs}k_{air}}{\rho C_p v_L} \left[(1 - \lambda_p)L_A \right], \quad (A14)$$

$$S_{\Theta V} = \frac{2g_{Ha}c_{PM}}{\rho C_p v_L} \left[LAD(1 - \lambda_p)(\bar{\Theta}_V - \bar{\Theta}) \right], \quad (A15)$$

where L_A [Wm^{-2}] is the absorbed flux density of longwave radiation in the canyon, ρ_{abs} [kgm^{-3}] is the density of absorbing molecules, k_{air} [m^2kg^{-1}] is their mass extinction cross section, $v_L = (1 - \lambda_p)$ [-] is the fraction of total volume that is outdoor air, g_{Ha} [$molm^{-2}s^{-1}$] is conductance for heat, c_{PM} [$Jmol^{-1}K^{-1}$] is the molar heat capacity for the air, and $\bar{\Theta}_V$ [K] is the temperature of tree foliage.

In the specific humidity Eqn. 16, the source/sink term can be calculated using the following equation

$$S_{QV} = \frac{\Lambda_M g_v \Omega}{\rho \Lambda v_L} \left[LAD(1 - \lambda_p) \left(s[\bar{\Theta}_V - \bar{\Theta}] + \frac{D}{P} \right) \right] \quad (A16)$$

where Λ_M [$Jmol^{-1}$] is molar latent heat of vaporization, Λ [Jkg^{-1}] is latent heat of vaporization, g_v [$molm^{-2}s^{-1}$] is the average surface and boundary-layer conductance for humidity for the whole leaf, s [K^{-1}] is derivative of saturation vapour pressure with respect to temperature divided by pressure, D [Pa] is the vapour deficit of the atmosphere, and P [Pa] is atmospheric pressure.

A3 Building Heat Exchanges

The heat fluxes in Eq. 17 can be parameterized as bellow

$$Q_{surf} = \Sigma h_i A_i (T_{si} - T_{in}) \quad (A17)$$

$$Q_{inf} = \dot{m}_{inf} C_p (T_{out} - T_{in}) \quad (A18)$$

$$Q_{vent} = \dot{m}_{vent} C_p (T_{supp} - T_{in}) \quad (A19)$$

where h_i [$Wm^{-2}K^{-1}$] is convective heat transfer coefficient (or u-value) for surface i and A_i [m^2m^{-2}] is surface area for surface i per building foot print area. Surface i can correspond to indoor elements such as ceiling, walls, floor, building mass, and windows. T_{si} [K] is the temperature of inner layer of elements, T_{in} [K] is indoor temperature, T_{out} [K] is the outdoor temperature averaged over building height, T_{supp} [K] is supply temperature, \dot{m}_{inf} [$kg s^{-1}m^{-2}$] is mass flow rate of infiltration (exfiltration) per building footprint area, and \dot{m}_{vent} [$kg s^{-1}m^{-2}$] is mass flow rate of ventilated air in the HVAC system per building footprint area.

25 A4 Radiation Model

A summary of details for the radiation model is provided here from Meili et al. (2020), while mathematical calculations are not provided here for brevity. The direct and diffuse shortwave radiation fluxes absorbed by each urban element are computed

as functions of urban canyon height, width, tree shape, and albedo. The urban geometry creates shading effects by blocking a portion of the incoming direct solar radiation flux. This flux is further decreased by the sky view factor, which reduces the incoming diffuse solar radiation flux and traps reflected solar rays within the canyon. Two steps are involved to calculate the net shortwave radiation flux: 1a) the direct shortwave radiation flux received by each urban element is calculated as a function of the sun position and shading effects created by buildings and trees; 1b) the diffuse shortwave radiation received by each urban element is computed as a function of the corresponding sky view factor; 2) infinite radiation reflections within the urban canyon are calculated using view factors and the net shortwave radiation flux for each urban element is then calculated. All urban elements are assumed to be Lambertian with isotropic scattering and reflections. If there are no trees, the view factors are computed analytically. Otherwise a Monte Carlo ray tracing algorithm is used. No obstructions are considered for roofs, i.e. trees cannot be taller than buildings. The model computes the net shortwave radiation flux due to both direct and diffuse radiation, allowing to investigate effects of shade and albedo in detail. The energy associated with the shortwave radiation exchange on each urban element is conserved.

For net longwave radiation flux on each urban surface, the difference between the incoming and outgoing longwave radiation fluxes are considered. These fluxes depend on surface temperatures. Infinite reflections of longwave radiation within the urban canyon are considered. Again, no obstructions are considered for roofs, i.e. trees cannot be taller than buildings. The canyon air does not impact the radiation exchange. The energy associated with the longwave radiation exchange on each urban surface is conserved.

For the case of no trees, analytical view factors are calculated using standard equations (Masson, 2000; Lee and Park, 2008; Ryu et al., 2011; Wang et al., 2013), while for trees the method of Ryu et al. (2016) is used. View factors meet a set of three requirements: 1) the self view factor of a flat surface is zero, 2) energy at the surface is conserved, and 3) view factors are reciprocal. The view factors for the case with trees are calculated using a Monte Carlo ray tracing algorithm (Wang, 2014; Frank et al., 2016). This algorithm performs a probabilistic sampling of all rays emitted by an urban element. The relative frequency of rays remitted by one element that hit another element is an estimation of the view factor between the two elements. On each element, a large number of randomly distributed emitting points are considered. These view factors are also corrected for the three requirements mentioned above.

Author contributions. MM wrote the paper with significant conceptual input from ESK and AAA and critical feedback from all co-authors. BB and LKN developed the base Urban Weather Generator (UWG) program in MATLAB. CM and SV translated UWG from MATLAB to Python. NN and ESK provided their code for the one-dimensional vertical diffusion model for the urban climate that was integrated into VCWG. MM and AAA developed the Vertical City Weather Generator (VCWG) program in Python by integrating various modeling components developed by BB, LKN, CM, SV, ESK, and NN. BD, AN, MKN, and MRN edited the manuscript.

Competing interests. The authors declare that they have no conflict of interest.

Acknowledgements. The computational platforms were set up with the assistance of Jeff Madge, Joel Best, and Matthew Kent at the University of Guelph. The authors thank Alberto Martilli at Centre for Energy, Environment and Technology (CIEMAT) in Madrid, Spain, who developed and shared an earlier version of the one-dimensional vertical diffusion model for the urban climate. The authors also thank Naika Meili at Institute of Environmental Engineering, ETH Zurich, Zurich, Switzerland, who developed and shared an earlier version of the urban radiation model.

This work was supported by the University of Guelph through the International Graduate Tuition Scholarship (IGTS) for the lead author; Discovery Grant program (401231) from the Natural Sciences and Engineering Research Council (NSERC) of Canada; Government of Ontario through the Ontario Centres of Excellence (OCE) under the Alberta-Ontario Innovation Program (AOIP) (053450); and Emission Reduction Alberta (ERA) (053498). OCE is a member of the Ontario Network of Entrepreneurs (ONE).

References

- Akbari, H., Pomerantz, M., and Taha, H.: Cool surfaces and shade trees to reduce energy use and improve air quality in urban areas, *Sol. Energy*, 70, 295–310, [https://doi.org/https://doi.org/10.1016/S0038-092X\(00\)00089-X](https://doi.org/https://doi.org/10.1016/S0038-092X(00)00089-X), 2001.
- Aliabadi, A. A., Krayenhoff, E. S., Nazarian, N., Chew, L. W., Armstrong, P. R., Afshari, A., and Norford, L. K.: Effects of
5 roof-edge roughness on air temperature and pollutant concentration in urban canyons, *Bound.-Lay. Meteorol.*, 164, 249–279, <https://doi.org/https://doi.org/10.1007/s10546-017-0246-1>, 2017.
- Aliabadi, A. A., Veriotes, N., and Pedro, G.: A Very Large-Eddy Simulation (VLES) model for the investigation of the neutral atmospheric boundary layer, *J. Wind Eng. Ind. Aerod.*, 183, 152–171, <https://doi.org/https://doi.org/10.1016/j.jweia.2018.10.014>, 2018.
- Aliabadi, A. A., Moradi, M., Clement, D., Lubitz, W. D., and Gharabaghi, B.: Flow and temperature dynamics in an urban canyon
10 under a comprehensive set of wind directions, wind speeds, and thermal stability conditions, *Environ. Fluid Mech.*, 19, 81–109, <https://doi.org/https://doi.org/10.1007/s10652-018-9606-8>, 2019.
- Armson, D., Stringer, P., and Ennos, A.: The effect of tree shade and grass on surface and globe temperatures in an urban area, *Urban For. Urban Gree.*, 11, 245–255, <https://doi.org/https://doi.org/10.1016/j.ufug.2012.05.002>, 2012.
- Basu, S. and Lacser, A.: A cautionary note on the use of Monin–Obukhov similarity theory in very high-resolution large-eddy simulations,
15 *Bound.-Lay. Meteorol.*, 163, 351–355, <https://doi.org/https://doi.org/10.1007/s10546-016-0225-y>, 2017.
- Bejarán, R. A. and Camilloni, I. A.: Objective method for classifying air masses: an application to the analysis of Buenos Aires’ (Argentina) urban heat island intensity, *Theor. Appl. Climatol.*, 74, 93–103, <https://doi.org/https://doi.org/10.1007/s00704-002-0714-4>, 2003.
- Blocken, B.: Computational Fluid Dynamics for urban physics: Importance, scales, possibilities, limitations and ten tips and tricks towards accurate and reliable simulations, *Build. Environ.*, 91, 219–245, <https://doi.org/https://doi.org/10.1016/j.buildenv.2015.02.015>, 2015.
- 20 Bornstein, R. D.: The two-dimensional URBMET urban boundary layer model, *J. Appl. Meteorol.*, 14, 1459–1477, [https://doi.org/https://doi.org/10.1175/1520-0450\(1975\)014<1459:TTDUUB>2.0.CO;2](https://doi.org/https://doi.org/10.1175/1520-0450(1975)014<1459:TTDUUB>2.0.CO;2), 1975.
- Britter, R. E. and Hanna, S. R.: Flow and dispersion in urban areas, *Annu. Rev. Fluid Mech.*, 35, 469–496, <https://doi.org/https://doi.org/10.1146/annurev.fluid.35.101101.161147>, 2003.
- Broadbent, A. M., Coutts, A. M., Nice, K. A., Demuzere, M., Krayenhoff, E. S., Tapper, N. J., and Wouters, H.: The Air-temperature
25 Response to Green/blue-infrastructure Evaluation Tool (TARGET v1. 0): an efficient and user-friendly model of city cooling, *Geosci. Model Dev.*, 12, 785–803, <https://doi.org/https://doi.org/10.5194/gmd-12-785-2019>, 2019.
- Bueno, B., Norford, L. K., Pigeon, G., and Britter, R.: Combining a detailed building energy model with a physically-based urban canopy model, *Bound.-Lay. Meteorol.*, 140, 471–489, <https://doi.org/https://doi.org/10.1007/s10546-011-9620-6>, 2011.
- Bueno, B., Norford, L. K., Hidalgo, J., and Pigeon, G.: The urban weather generator, *J. Build. Perf. Simulat.*, 6, 269–281,
30 <https://doi.org/https://doi.org/10.1080/19401493.2012.718797>, 2012a.
- Bueno, B., Pigeon, G., Norford, L. K., Zibouche, K., and Marchadier, C.: Development and evaluation of a building energy model integrated in the TEB scheme, *Geosci. Model Dev.*, 5, 433–448, <https://doi.org/https://doi.org/10.5194/gmd-5-433-2012>, 2012, 2012b.
- Bueno, B., Roth, M., Norford, L. K., and Li, R.: Computationally efficient prediction of canopy level urban air temperature at the neighbourhood scale, *Urban Climate*, 9, 35–53, <https://doi.org/https://doi.org/10.1016/j.uclim.2014.05.005>, 2014.
- 35 Businger, J. A., Wyngaard, J. C., Izumi, Y., and Bradley, E. F.: Flux-profile relationships in the atmospheric surface layer, *J. Atmos. Sci.*, 28, 181–189, [https://doi.org/https://doi.org/10.1175/1520-0469\(1971\)028<0181:FPRITA>2.0.CO;2](https://doi.org/https://doi.org/10.1175/1520-0469(1971)028<0181:FPRITA>2.0.CO;2), 1971.

- Chen, F., Kusaka, H., Bornstein, R., Ching, J., Grimmond, C. S. B., Grossman-Clarke, S., Loridan, T., Manning, K. W., Martilli, A., Miao, S., Sailor, D., Salamanca, F. P., Taha, H., Tewari, M., Wang, X., Wyszogrodzki, A. A., and Zhang, C.: The integrated WRF/urban modelling system: development, evaluation, and applications to urban environmental problems, *Int. J. Climatol.*, 31, 273–288, <https://doi.org/https://doi.org/10.1002/joc.2158>, 2011.
- 5 Chin, H.-N. S., Leach, M. J., Sugiyama, G. A., Leone Jr, J. M., Walker, H., Nasstrom, J., and Brown, M. J.: Evaluation of an urban canopy parameterization in a mesoscale model using VTMX and URBAN 2000 Data, *Mon. Weather Rev.*, 133, 2043–2068, <https://doi.org/https://doi.org/10.1175/MWR2962.1>, 2005.
- Christen, A. and Vogt, R.: Energy and radiation balance of a central European city, *Int. J. Climatol.*, 24, 1395–1421, <https://doi.org/https://doi.org/10.1002/joc.1074>, 2004.
- 10 Coutts, A. M., Beringer, J., and Tapper, N. J.: Impact of increasing urban density on local climate: spatial and temporal variations in the surface energy balance in Melbourne, Australia, *J. Appl. Meteorol. Clim.*, 46, 477–493, <https://doi.org/https://doi.org/10.1175/JAM2462.1>, 2007.
- Crank, P. J., Sailor, D. J., Ban-Weiss, G., and Taleghani, M.: Evaluating the ENVI-met microscale model for suitability in analysis of targeted urban heat mitigation strategies, *Urban climate*, 26, 188–197, <https://doi.org/https://doi.org/10.1016/j.uclim.2018.09.002>, 2018.
- Dupont, S., Otte, T. L., and Ching, J. K. S.: Simulation of meteorological fields within and above urban and rural canopies with a mesoscale model, *Bound.-Lay. Meteorol.*, 113, 111–158, <https://doi.org/https://doi.org/10.1023/B:BOUN.0000037327.19159.ac>, 2004.
- 15 Dyer, A. J.: A review of flux-profile relationships, *Bound.-Lay. Meteorol.*, 7, 363–372, <https://doi.org/https://doi.org/10.1007/BF00240838>, 1974.
- Emmanuel, R. and Steemers, K.: Connecting the realms of urban form, density and microclimate, *Build. Res. Inf.*, 46, 804–808, <https://doi.org/https://doi.org/10.1080/09613218.2018.1507078>, 2018.
- 20 Erell, E. and Williamson, T.: Simulating air temperature in an urban street canyon in all weather conditions using measured data at a reference meteorological station, *Int. J. Climatol.*, 26, 1671–1694, <https://doi.org/https://doi.org/10.1002/joc.1328>, 2006.
- Frank, A., Heidemann, W., and Spindler, K.: Modeling of the surface-to-surface radiation exchange using a Monte Carlo method, *Journal of Physics: Conference Series*, 745, 032 143, 2016.
- Giometto, M. G., Christen, A., Egli, P. E., Schmid, M. F., Tooke, R., Coops, N. C., and Parlange, M. B.: Effects of trees on mean wind, turbulence and momentum exchange within and above a real urban environment, *Adv. Water Resour.*, 106, 154–168, <https://doi.org/https://doi.org/10.1016/j.advwatres.2017.06.018>, 2017.
- 25 Gowardhan, A. A., Pardyjak, E. R., Senocak, I., and Brown, M. J.: A CFD-based wind solver for an urban fast response transport and dispersion model, *Environ. Fluid Mech.*, 11, 439–464, <https://doi.org/https://doi.org/10.1007/s10652-011-9211-6>, 2011.
- Grimmond, C. S. B. and Oke, T. R.: Aerodynamic properties of urban areas derived from analysis of surface form, *J. Appl. Meteorol.*, 38, 1262–1292, [https://doi.org/https://doi.org/10.1175/1520-0450\(1999\)038<1262:APOUAD>2.0.CO;2](https://doi.org/https://doi.org/10.1175/1520-0450(1999)038<1262:APOUAD>2.0.CO;2), 1999.
- 30 Grimmond, C. S. B., Souch, C., and Hubble, M. D.: Influence of tree cover on summertime surface energy balance fluxes, San Gabriel Valley, Los Angeles, *Clim. Res.*, 6, 45–57, 1996.
- Gros, A., Bozonnet, E., and Inard, C.: Cool materials impact at district scale: Coupling building energy and microclimate models, *Sustain. Cities Soc.*, 13, 254–266, <https://doi.org/https://doi.org/10.1016/j.scs.2014.02.002>, 2014.
- 35 Hamdi, R. and Masson, V.: Inclusion of a drag approach in the Town Energy Balance (TEB) Scheme: Offline 1D Evaluation in a Street Canyon, *J. Appl. Meteorol. Clim.*, 47, 2627–2644, <https://doi.org/https://doi.org/10.1175/2008JAMC1865.1>, 2008.

- Ho, H. C., Knudby, A., Xu, Y., Hodul, M., and Aminipouri, M.: A comparison of urban heat islands mapped using skin temperature, air temperature, and apparent temperature (Humidex), for the greater Vancouver area, *Sci. Total Environ.*, 544, 929–938, <https://doi.org/10.1016/j.scitotenv.2015.12.021>, 2016.
- Jamei, E., Rajagopalan, P., Seyedmahmoudian, M., and Jamei, Y.: Review on the impact of urban geometry and pedestrian level greening on outdoor thermal comfort, *Renew. Sust. Energ. Rev.*, 54, 1002–1017, <https://doi.org/https://doi.org/10.1016/j.rser.2015.10.104>, 2016.
- Joffre, S. M., Kangas, M., Heikinheimo, M., and Kitaigorodskii, S. A.: Variability of the stable and unstable atmospheric boundary-layer height and its scales over a Boreal forest, *Bound.-Lay. Meteorol.*, 99, 429–450, <https://doi.org/https://doi.org/10.1023/A:1018956525605>, 2001.
- Kastner-Klein, P., Berkowicz, R., and Britter, R.: The influence of street architecture on flow and dispersion in street canyons, *Meteorol. Atmos. Phys.*, 87, 121–131, <https://doi.org/https://doi.org/10.1007/s00703-003-0065-4>, 2004.
- Kikegawa, Y., Genchi, Y., Yoshikado, H., and Kondo, H.: Development of a numerical simulation system toward comprehensive assessments of urban warming countermeasures including their impacts upon the urban buildings' energy-demands, *Appl. Energ.*, 76, 449–466, [https://doi.org/https://doi.org/10.1016/S0306-2619\(03\)00009-6](https://doi.org/https://doi.org/10.1016/S0306-2619(03)00009-6), 2003.
- Kleerekoper, L., van Esch, M., and Salcedo, T. B.: How to make a city climate-proof, addressing the urban heat island effect, *Resour. Conserv. Recy.*, 64, 30–38, <https://doi.org/https://doi.org/10.1016/j.resconrec.2011.06.004>, 2012.
- Kochanski, A. K., Pardyjak, E. R., Stoll, R., Gowardhan, A., Brown, M. J., and Steenburgh, W. J.: One-way coupling of the WRF-QUIC urban dispersion modeling system, *J. Appl. Meteorol. Clim.*, 54, 2119–2139, <https://doi.org/https://doi.org/10.1175/JAMC-D-15-0020.1>, 2015.
- Kondo, H., Genchi, Y., Kikegawa, Y., Ohashi, Y., Yoshikado, H., and Komiyama, H.: Development of a multi-layer urban canopy model for the analysis of energy consumption in a big city: structure of the urban canopy model and its basic performance, *Bound.-Lay. Meteorol.*, 116, 395–421, <https://doi.org/https://doi.org/10.1007/s10546-005-0905-5>, 2005.
- Kono, T., Ashie, Y., and Tamura, T.: Mathematical derivation of spatially-averaged momentum equations for an urban canopy model using underlying concepts of the immersed boundary method, *Bound.-Lay. Meteorol.*, 135, 185–207, <https://doi.org/https://doi.org/10.1007/s10546-010-9475-2>, 2010.
- Krayenhoff, E., Christen, A., Martilli, A., and Oke, T.: A multi-layer radiation model for urban neighbourhoods with trees, *Bound.-Lay. Meteorol.*, 151, 139–178, <https://doi.org/https://doi.org/10.1007/s10546-013-9883-1>, 2014.
- Krayenhoff, E. S.: A multi-layer urban canopy model for neighbourhoods with trees, Ph.D. thesis, University of British Columbia, <https://doi.org/10.14288/1.0167084>, 2014.
- Krayenhoff, E. S. and Voogt, J. A.: A microscale three-dimensional urban energy balance model for studying surface temperatures, *Bound.-Layer Meteorol.*, 123, 433–461, <https://doi.org/https://doi.org/10.1007/s10546-006-9153-6>, 2007.
- Krayenhoff, E. S., Santiago, J.-L., Martilli, A., Christen, A., and Oke, T. R.: Parametrization of drag and turbulence for urban neighbourhoods with trees, *Bound.-Lay. Meteorol.*, 156, 157–189, <https://doi.org/https://doi.org/10.1007/s10546-015-0028-6>, 2015.
- Krayenhoff, E. S., Jiang, T., Christen, A., Martilli, A., Oke, T. R., Bailey, B. N., Nazarian, N., Voogt, J. A., Giometto, M. G., Stastny, A., et al.: A multi-layer urban canopy meteorological model with trees (BEP-Tree): Street tree impacts on pedestrian-level climate, *Urban Climate*, 32, 100590, <https://doi.org/https://doi.org/10.1016/j.uclim.2020.100590>, 2020.
- Kusaka, H., Kondo, H., Kikegawa, Y., and Kimura, F.: A simple single-layer urban canopy model for atmospheric models: comparison with multi-layer and slab models, *Bound.-Lay. Meteorol.*, 101, 329–358, <https://doi.org/https://doi.org/10.1023/A:1019207923078>, 2001.

- Kusaka, H., Hara, M., and Takane, Y.: Urban climate projection by the WRF model at 3-km horizontal grid increment: dynamical downscaling and predicting heat stress in the 2070's August for Tokyo, Osaka, and Nagoya metropolises, *J. Meteorol. Soc. Jpn. Ser. II*, 90, 47–63, <https://doi.org/https://doi.org/10.2151/jmsj.2012-B04>, 2012.
- Leal Filho, W., Echevarria Icaza, L., Emanche, V. O., and Quasem Al-Amin, A.: An evidence-based review of impacts, strategies and tools to mitigate urban heat islands, *Int. J. Env. Res. Pub. He.*, 14, 1600, <https://doi.org/https://doi.org/10.3390/ijerph14121600>, 2017.
- Lee, S.-H. and Park, S.-U.: A vegetated urban canopy model for meteorological and environmental modelling, *Bound.-Lay. Meteorol.*, 126, 73–102, <https://doi.org/https://doi.org/10.1007/s10546-007-9221-6>, 2008.
- Lesnikowski, A.: Adaptation to urban heat island effect in Vancouver, BC: A case study in analyzing vulnerability and adaptation opportunities, Ph.D. thesis, University of British Columbia, <https://doi.org/10.14288/1.0075852>, 2014.
- 10 Loughner, C. P., Allen, D. J., Zhang, D.-L., Pickering, K. E., Dickerson, R. R., and Landry, L.: Roles of urban tree canopy and buildings in urban heat island effects: parameterization and preliminary results, *J. Appl. Meteorol. Clim.*, 51, 1775–1793, <https://doi.org/https://doi.org/10.1175/JAMC-D-11-0228.1>, 2012.
- Louis, J.-F.: A parametric model of vertical eddy fluxes in the atmosphere, *Bound.-Lay. Meteorol.*, 17, 187–202, <https://doi.org/https://doi.org/10.1007/BF00117978>, 1979.
- 15 Lundquist, K. A., Chow, F. K., and Lundquist, J. K.: An immersed boundary method for the weather research and forecasting model, *Mon. Weather Rev.*, 138, 796–817, <https://doi.org/https://doi.org/10.1175/2009MWR2990.1>, 2010.
- Mahura, A., Baklanov, A., Petersen, C., Nielsen, N. W., and Amstrup, B.: Verification and case studies for urban effects in HIRLAM numerical weather forecasting, in: *Meteorological and Air Quality Models for Urban Areas*, pp. 143–150, Springer, Berlin, https://doi.org/https://doi.org/10.1007/978-3-642-00298-4_14, 2009.
- 20 Maronga, B., Gryschka, M., Heinze, R., Hoffmann, F., Kanani-Sühring, F., Keck, M., Ketelsen, K., Letzel, M. O., Sühring, M., and Raasch, S.: The Parallelized Large-Eddy Simulation Model (PALM) version 4.0 for atmospheric and oceanic flows: model formulation, recent developments, and future perspectives, *Geosci. Model Dev.*, 8, 2515–2551, <https://doi.org/https://doi.org/10.5194/gmd-8-2515-2015>, 2015.
- Martilli, A. and Santiago, J. L.: CFD simulation of airflow over a regular array of cubes. Part II: analysis of spatial average properties, *Bound.-Lay. Meteorol.*, 122, 635–654, <https://doi.org/https://doi.org/10.1007/s10546-006-9124-y>, 2007.
- 25 Martilli, A., Clappier, A., and Rotach, M. W.: An urban surface exchange parameterisation for mesoscale models, *Bound.-Lay. Meteorol.*, 104, 261–304, <https://doi.org/https://doi.org/10.1023/A:1016099921195>, 2002.
- Masson, V.: A physically-based scheme for the urban energy budget in atmospheric models, *Bound.-Lay. Meteorol.*, 94, 357–397, <https://doi.org/https://doi.org/10.1023/A:1002463829265>, 2000.
- Masson, V., Grimmond, C. S. B., and Oke, T. R.: Evaluation of the Town Energy Balance (TEB) scheme with direct measurements from dry districts in two cities, *J. Appl. Meteorol.*, 41, 1011–1026, [https://doi.org/https://doi.org/10.1175/1520-0450\(2002\)041<1011:EOTTEB>2.0.CO;2](https://doi.org/https://doi.org/10.1175/1520-0450(2002)041<1011:EOTTEB>2.0.CO;2), 2002.
- Masson, V., Gomes, L., Pigeon, G., Liousse, C., Pont, V., Lagouarde, J. P., Voogt, J., Salmond, J., Oke, T. R., Hidalgo, J., Legain, D., Garrouste, O., Lac, C., Connan, O., Briottet, X., Lachérade, S., and Tulet, P.: The Canopy and Aerosol Particles Interactions in Toulouse Urban Layer (CAPITOU) experiment, *Meteorol. Atmos. Phys.*, 102, 135–157, <https://doi.org/https://doi.org/10.1007/s00703-008-0289-4>,
35 2008.
- Mauree, D., Blond, N., and Clappier, A.: Multi-scale modeling of the urban meteorology: Integration of a new canopy model in the WRF model, *Urban Climate*, 26, 60–75, <https://doi.org/https://doi.org/10.1016/j.uclim.2018.08.002>, 2018.

- Meili, N., Manoli, G., Burlando, P., Bou-Zeid, E., Chow, W. T. L., Coutts, A. M., Daly, E., Nice, K. A., Roth, M., Tapper, N. J., Velasco, E., Vivoni, E. R., and Faticchi, S.: An urban ecohydrological model to quantify the effect of vegetation on urban climate and hydrology (UT&C v1.0), *Geosci. Model Dev.*, 13, 335–362, <https://doi.org/https://doi.org/10.5194/gmd-13-335-2020>, 2020.
- Mills, G.: An urban canopy-layer climate model, *Theor. Appl. Climatol.*, 57, 229–244, <https://doi.org/https://doi.org/10.1007/BF00863615>,
5 1997.
- Moeng, C.-H., Dudhia, J., Klemp, J., and Sullivan, P.: Examining two-way grid nesting for large eddy simulation of the PBL using the WRF model, *Mon. Weather Rev.*, 135, 2295–2311, <https://doi.org/https://doi.org/10.1175/MWR3406.1>, 2007.
- Monin, A. S. and Obukhov, A. M.: Basic regularity in turbulent mixing in the surface layer of the atmosphere, *Tr. Akad. Nauk SSSR Geophys. Inst.*, 1957.
- 10 Nazarian, N. and Kleissl, J.: Realistic solar heating in urban areas: air exchange and street-canyon ventilation, *Build. Environ.*, 95, 75–93, <https://doi.org/https://doi.org/10.1016/j.buildenv.2015.08.021>, 2016.
- Nazarian, N., Martilli, A., and Kleissl, J.: Impacts of realistic urban heating, Part I: spatial variability of mean flow, turbulent exchange and pollutant dispersion, *Bound.-Lay. Meteorol.*, 166, 367–393, <https://doi.org/https://doi.org/10.1007/s10546-017-0311-9>, 2018.
- Nazarian, N., Krayenhoff, E. S., and Martilli, A.: A one-dimensional model of turbulent flow through “urban” canopies (MLUCM v2.0): up-
15 dates based on large-eddy simulation, *Geosci. Model Dev.*, 13, 937–953, <https://doi.org/https://doi.org/10.5194/gmd-13-937-2020>, 2020.
- Oke, T. R., Mills, G., Christen, A., and Voogt, J. A.: *Urban Climates*, Cambridge University Press, London, <https://doi.org/https://doi.org/10.1017/9781139016476>, 2017.
- Paulson, C. A.: The mathematical representation of wind speed and temperature profiles in the unstable atmospheric surface layer, *J. Appl. Meteorol.*, 9, 857–861, [https://doi.org/https://doi.org/10.1175/1520-0450\(1970\)009<0857:TMROWS>2.0.CO;2](https://doi.org/https://doi.org/10.1175/1520-0450(1970)009<0857:TMROWS>2.0.CO;2), 1970.
- 20 Pope, S. B.: *Turbulent flows*, Cambridge University Press, Cambridge, <https://doi.org/https://doi.org/10.1017/CBO9780511840531>, 2000.
- Redon, E. C., Lemonsu, A., Masson, V., Morille, B., and Musy, M.: Implementation of street trees within the solar radiative exchange parameterization of TEB in SURFEX v8.0, *Geosci. Model Dev.*, 10, 385–411, <https://doi.org/https://doi.org/10.5194/gmd-10-385-2017>, 2017.
- Resler, J., Krč, P., Belda, M., Juruš, P., Benešová, N., Lopata, J., Vlček, O., Damašková, D., Eben, K., Derbek, P., Maronga, B., and Kanani-
25 Sühling, F.: PALM-USM v1. 0: A new urban surface model integrated into the PALM large-eddy simulation model, *Geosci. Model Dev.*, 10, 3635–3659, <https://doi.org/https://doi.org/10.5194/gmd-10-3635-2017>, 2017.
- Rotach, M. W., Vogt, R., Bernhofer, C., Batchvarova, E., Christen, A., Clappier, A., Feddersen, B., Gryning, S. E., Martucci, G., Mayer, H., Mitev, V., Oke, T. R., Parlow, E., Richner, H., Roth, M., Roulet, Y. A., Ruffieux, D., Salmond, J. A., Schatzmann, M., and Voogt, J. A.: BUBBLE—an Urban boundary layer meteorology project, *Theor. Appl. Climatol.*, 81, 231–261,
30 <https://doi.org/https://doi.org/10.1007/s00704-004-0117-9>, 2005.
- Roth, M.: Review of atmospheric turbulence over cities, *Q. J. R. Meteorol. Soc.*, 126, 941–990, <https://doi.org/https://doi.org/10.1002/qj.49712656409>, 2000.
- Runnalls, K. E. and Oke, T. R.: Dynamics and controls of the near-surface heat island of Vancouver, British Columbia, *Physical Geography*, 21, 283–304, <https://doi.org/https://doi.org/10.1080/02723646.2000.10642711>, 2000.
- 35 Ryu, Y.-H., Baik, J.-J., and Lee, S.-H.: A new single-layer urban canopy model for use in mesoscale atmospheric models, *J. Appl. Meteorol. Clim.*, 50, 1773–1794, <https://doi.org/https://doi.org/10.1175/2011JAMC2665.1>, 2011.
- Ryu, Y.-H., Bou-Zeid, E., Wang, Z.-H., and Smith, J. A.: Realistic representation of trees in an urban canopy model, *Bound.-Lay. Meteorol.*, 159, 193–220, <https://doi.org/https://doi.org/10.1007/s10546-015-0120-y>, 2016.

- Salamanca, F., Krpo, A., Martilli, A., and Clappier, A.: A new building energy model coupled with an urban canopy parameterization for urban climate simulations—part I. formulation, verification, and sensitivity analysis of the model, *Theor. Appl. Climatol.*, 99, 331–344, <https://doi.org/https://doi.org/10.1007/s00704-009-0142-9>, 2010.
- 5 Salamanca, F., Georgescu, M., Mahalov, A., Moustaoi, M., and Wang, M.: Anthropogenic heating of the urban environment due to air conditioning, *J. Geophys. Res.-Atmos.*, 119, 5949–5965, <https://doi.org/https://doi.org/10.1002/2013JD021225>, 2014.
- Saneinejad, S., Moonen, P., Defraeye, T., Derome, D., and Carmeliet, J.: Coupled CFD, radiation and porous media transport model for evaluating evaporative cooling in an urban environment, *J. Wind. Eng. Ind. Aerodyn.*, 104-106, 455–463, <https://doi.org/https://doi.org/10.1016/j.jweia.2012.02.006>, 2012.
- 10 Santiago, J. L. and Martilli, A.: A dynamic urban canopy parameterization for mesoscale models based on computational fluid dynamics Reynolds-Averaged Navier-Stokes microscale simulations, *Bound.-Lay. Meteorol.*, 137, 417–439, <https://doi.org/10.1007/s10546-010-9538-4>, 2010.
- Santiago, J. L., Krayenhoff, E. S., and Martilli, A.: Flow simulations for simplified urban configurations with microscale distributions of surface thermal forcing, *Urban Climate*, 9, 115–133, <https://doi.org/https://doi.org/10.1016/j.uclim.2014.07.008>, 2014.
- 15 Simón-Moral, A., Santiago, J. L., and Martilli, A.: Effects of unstable thermal stratification on vertical fluxes of heat and momentum in urban areas, *Bound.-Lay. Meteorol.*, 163, 103–121, <https://doi.org/10.1007/s10546-016-0211-4>, 2017.
- Souch, C. A. and Souch, C.: The effect of trees on summertime below canopy urban climates: a case study Bloomington, Indiana, *J. Arboriculture*, 19, 303–312, 1993.
- Soulhac, L., Salizzoni, P., Cierco, F.-X., and Perkins, R.: The model SIRANE for atmospheric urban pollutant dispersion; part I, presentation of the model, *Atmos. Environ.*, 45, 7379–7395, <https://doi.org/https://doi.org/10.1016/j.atmosenv.2011.07.008>, 2011.
- 20 Stull, R. B.: An introduction to boundary layer meteorology, Kluwer Academic Publishers, Dordrecht, The Netherlands, <https://doi.org/10.1007/978-94-009-3027-8>, 1988.
- Talbot, C., Bou-Zeid, E., and Smith, J.: Nested mesoscale large-eddy simulations with WRF: performance in real test cases, *J. Hydrometeorol.*, 13, 1421–1441, <https://doi.org/https://doi.org/10.1175/JHM-D-11-048.1>, 2012.
- 25 Tseng, Y.-H., Meneveau, C., and Parlange, M. B.: Modeling flow around bluff bodies and predicting urban dispersion using large eddy simulation, *Environ. Sci. Technol.*, 40, 2653–2662, <https://doi.org/https://doi.org/10.1021/es051708m>, 2006.
- Wang, C., Wang, Z.-H., and Yang, J.: Cooling effect of urban trees on the built environment of contiguous United States, *Earth’s Future*, 6, 1066–1081, <https://doi.org/https://doi.org/10.1029/2018EF000891>, 2018.
- 30 Wang, H., Skamarock, W. C., and Feingold, G.: Evaluation of scalar advection schemes in the advanced research WRF model using large-eddy simulations of aerosol-cloud interactions, *Mon. Weather Rev.*, 137, 2547–2558, <https://doi.org/https://doi.org/10.1175/2009MWR2820.1>, 2009.
- Wang, Z.-H.: Geometric effect of radiative heat exchange in concave structure with application to heating of steel I-sections in fire, *Int. J. Heat Mass Tran.*, 53, 997–1003, <https://doi.org/https://doi.org/10.1016/j.ijheatmasstransfer.2009.11.013>, 2010.
- Wang, Z.-H.: Monte Carlo simulations of radiative heat exchange in a street canyon with trees, *Sol. Energy*, 110, 704 – 713, <https://doi.org/https://doi.org/10.1016/j.solener.2014.10.012>, 2014.
- 35 Wang, Z.-H., Bou-Zeid, E., and Smith, J. A.: A coupled energy transport and hydrological model for urban canopies evaluated using a wireless sensor network, *Q. J. Roy. Meteor. Soc.*, 139, 1643–1657, <https://doi.org/https://doi.org/10.1002/qj.2032>, 2013.
- Wong, M. S., Nichol, J. E., To, P. H., and Wang, J.: A simple method for designation of urban ventilation corridors and its application to urban heat island analysis, *Build. Environ.*, 45, 1880–1889, <https://doi.org/https://doi.org/10.1016/j.buildenv.2010.02.019>, 2010.

- Yaghoobian, N. and Kleissl, J.: Effect of reflective pavements on building energy use, *Urban Climate*, 2, 25–42, <https://doi.org/https://doi.org/10.1016/j.uclim.2012.09.002>, 2012.
- Yang, X. and Li, Y.: The impact of building density and building height heterogeneity on average urban albedo and street surface temperature, *Build. Environ.*, 90, 146–156, <https://doi.org/https://doi.org/10.1016/j.buildenv.2015.03.037>, 2015.
- 5 Yuan, C., Norford, L. K., and Ng, E.: A semi-empirical model for the effect of trees on the urban wind environment, *Landscape Urban Plan.*, 168, 84–93, <https://doi.org/https://doi.org/10.1016/j.landurbplan.2017.09.029>, 2017.
- Zajic, D., Fernando, H. J. S., Calhoun, R., Princevac, M., Brown, M. J., and Pardyjak, E. R.: Flow and turbulence in an urban canyon, *J. Appl. Meteorol. Clim.*, 50, 203–223, <https://doi.org/https://doi.org/10.1175/2010JAMC2525.1>, 2011.
- Zeng, X. and Dickinson, R. E.: Effect of surface sublayer on surface skin temperature and fluxes, *Journal of Climate*, 11, 537–550,
10 [https://doi.org/https://doi.org/10.1175/1520-0442\(1998\)011<0537:EOSSOS>2.0.CO;2](https://doi.org/https://doi.org/10.1175/1520-0442(1998)011<0537:EOSSOS>2.0.CO;2), 1998.